An Extended Fully-Implicit Hybrid Model for Geological CO2 Storage

Master Thesis

Student: Vetle Nevland

Supervisors: Knut-Andreas Lie, Odd Andersen, Halvor Møll Nilsen, SINTEF

December 24, 2022

Contents

1   Introduction

The past decade, consequences of accumulated greenhouse gas emission have materialized across the globe and the severeness of the climate crisis is indisputable. A promising initiative for mitigating the ongoing climate change is CO2 capture and storage, a technology that has been active and developed over several decades. This thesis will particularly investigate the Sleipner field, where over 16 megaton of CO2 has been injected since 1996. Geophysical monitoring has provided valuable insight to address the potential for CO2 storage at Sleipner, including data of the layered structure as well as the migrating CO2 plume [2]. Simulations from models tailored towards CO2 storage can be tested against in-situ measurements in order to tune the model parameters and improve the accuracy of the model, as done in the following study [42].

Injected CO2 should preferentially be trapped inside the reservoir indefinitely. The leakage potential constitute many factors including reservoir geometries and properties, as well as operational management such as injection rates and bottom-hole pressure. Finding an optimal injection site that maximizes CO2 storage and minimizes leakage is not trivial, and numerical modelling is inevitable to answer these questions. 25 years of real data is not sufficient to build a full-scale model for CO2 storage, stressing the need for long-term numerical simulations. Traditional reservoir simulators are usually applied on reservoirs of only a few kilometers in lateral extent and operate for a couple of decades. As for long-term storage, injected CO2 should preferably spread widely throughout the reservoir in order to utilize as much pore space as possible and minimize leakage. Thus, CO2 storage requires simulators that work with lateral dimensions of several hundred kilometers. Moreover, injected CO2 should be safely stored not only for decades but for millennia. In other words, enormous spatial *and* temporal scales are necessary for a reliable 3D simulator for CO2 storage. Compared to conventional 3D reservoir simulators, this poses an almost intractable computational challenge [24]. At the top of this, the governing equations for multiphase flow in porous media are strongly coupled with multiple variables having a highly nonlinear dependence, requiring expensive iterative numerical schemes to advance the solution forward in time. There are currently no available simulators that solve the fully coupled system of equations without decoupling and concealing relevant processes from the mathematical description [14]. Alternative measures are required. To this end, several assumptions and simplifications have been applied on the conventional simulators, achieving great accuracy [33]. A successful approach is the assumption of vertical equilibrium (VE) during migration of CO2, which amounts to reducing the spatial dimensions to two, thereby facilitating faster computations.

Despite the VE models achieving great accuracy, often comparable to full 3D simulators, their application is limited to idealized scenarios where the phases quickly segregate in the vertical direction. In regions of more complex flow behaviour, e.g. close to wells, and a long time scale for fluid segregation, the assumption of vertical equilibrium is not justified [15], and the predicted

migration paths are more prone to errors. To circumvent this issue, hybrid models have been developed the last couple of years, increasing accuracy with (in many cases) an acceptable sacrifice in computational requirements. The idea is to combine the power from VE and full-scale models, by applying 3D models in complex regions requiring special treatment and VE models in remaining regions where the assumption of vetical segregation is justified [36]. Compared to pure VE, hybrid models have shown to provide results closer to a conventional 3D simulator [36], [9]. The convenience of hybrid models is substantiated from the fact that geological data of deep saline aquifers is scarce, consequently yielding large uncertainties in petrophysical parameters. Stochastic realizations of the reservoir is thus an inevitable demand, but this is infeasible for full-dimensional models. Fortunately, the significant reduction in runtime makes stochastic simulations of hybrid models practical [42].

The Utsira formation of the Sleipner field primarily consist of very high-permeable sandstone and large porosities [13]. Injected CO_2 thus has a high potential to spread and vertical segregation with the resident brine is expected to occur quickly enough for the capillary fringe separating CO_2 and brine to be of negligable thickness. These regions are well suited for sharp interface vertical equilibrium models [14, pp. 23]. On the other hand, an abundance of thin, low-permeable layers of shale are embedded into the high-permeable formation where CO_2 accumulate and vertical migration is severely retarded [2]. The assumption of vertical equilibrium is not appropriate here and a full-dimensional subdomain is generally desired to resolve the local flow. The Utsira formation is therefore an excellent candidate for a hybrid framework to simulate CO_2 migration, combining simplified VE models with full-dimensional models [2].

Hybrid models serve as a great tradeoff between VE models and fine-scale 3D models, but some modeling aspects remain elusive, for example diffuse leakage. [36] touched upon the effect of diffuse leakage, but flow behavior internally in shales was not resolved. Moreover, since diffuse leakage is subject to modeling improvements, comprehensive studies analysing the sensitivity of CO_2 migration to distribution of semi-permeable layers in a multilayered system give novel and valuable insight. The applicability of hybrid models is ultimately dependent on the relevant time scale for the problem, the spatial and temporal balance of forces as well as appropriate spatial resolution to capture flow behavior in layers of different rock characteristics [21].

Multiple variants of hybrid models have been established in the scientific community, the differences being primarily the numerical schemes and representation of reduced dimensions. [36] studied long-term CO_2 storage in multilayered systems by coupling a full-dimensional 3D model with stacked VE models in a fully-implicit numerical setup. Other studies ([21], [46]) have developed hybrid models by combining a full-dimensional model with apparent VE columns where vertical flow is resolved as an isolated one-dimensional problem. The IMPES scheme is used to solve the flow equations numerically by decoupling the pressure and transport equations, facilitating cheaper computations although limited by a time step restriction.

4

While the frameworks show promising results compared to conventional VE models, the scenarios investigated are of limited complexity. While the IMPES framework in [46] included a capillary fringe and residual brine saturation to facilitate real storage scenarios, studies based on a fully-implicit solution scheme [36] assume a sharp interface with negligable entry pressure and no residual saturations. Hence, it would be valuable to further develop the fully-implicit hybrid model by implementing these physical effects.

Another area of improvement is appropriate modelling of flow through nearly impermeable layers. The hybrid model in [36] represented sealing layers as lower-dimensional faces in the grid, adjusting their transmissibility by multipliers to account for diffuse leakage of brine through a confining layer. However, if the sealing layers are deep enough internal flow behavior and pressure gradients across the layer become important, but this information is lost in a face-representation. An alternative is to represent the layers as full-dimensional cells. This has the benefit of resolving any flow internally in the sealing layers by inclusion of pressure gradients that drive the flow. Numerically, a full-dimensional representation is obviously more challenging, but the relevant low-permeable layers are much thinner than the vertical extent of the formation, thus the hybrid model is still significantly less complex than the full-dimensional model. In return, results of hybrid models are in excellent agreement with full-dimensional models for injection scenarios of medium complexity while running orders of magnitude faster [36], [9].

The open-source software MRST [37] provides a module `hybrid-ve` specific for application of hybrid models, based on a fully-implicit numerical solution scheme and automatic detection of different discretization regions in the hybrid domain. An essential part of this thesis is devoted to extend the hybrid model with currently missing physical effects such as residual saturation and capillary pressure, which have shown to have a great impact on the migrating plume and long-term trapping [18]. Also, possibility of improved modelling of diffuse leakage will be addressed by considering multilayered reservoir systems. We commence with case studies on two-dimensional and three-dimensional fictitious domains of various complexity, merely to present the novel hybrid framework, and later proceed with a case study on a section of the (real) Utsira formation, an excellent candidate for modeling diffuse leakage due to its multilayered characteristics [13]. The implementation of residual saturation will give valuable insight to distribution of CO2, as studies have shown that residual saturation has a major impact on long-term trapping of CO2 in the Utsira formation [14].

2 Theory

2.1 Physical description

Similar to traditional reservoir simulation, CO2 storage involves the study of flow in porous media. In this regard, we are considering the joint flow of CO2 and brine, labeled multiphase flow. The purpose of this chapter is to provide a concise description of the physics behind multiphase flow, in particular the properties of fluids and rocks and the governing equations.

2.1.1 Force balance

Fluids in the subsurface are subject to different forces, and the balance of these forces govern the movement of the fluids. For multiphase flow, particularly a two-phase CO2-brine system, there are primarily three dominating forces; buoyant, capillary and viscous forces [45]. The balance depends on multiple factors, including spatial and temporal scales, formation geometry and flow rates. For high flow rates, the effect of viscous forces is dominating and the system is considered to be in the Darcy flow regime, attributable to significant pressure gradients [22]. In contrast, for low flow rates viscous forces weaken and the effect of density is emphasized. The system approaches the capillary flow regime, attributable to distinct migration paths and capillary forces at the fluid-fluid interface. Addressing the force balance allows distinguishing regions of different flow regimes, a characterization that is important when it comes to numerical modeling because certain regimes justify certain simplifications.

Viscous forces tend to dominate early in the injection stage when local pressure gradients are large, while capillary forces are diffusive and typically become prevalent in the post-injection stage. For CO2 storage, gravity is the long-term dominating force, although reservoir geometry significantly impacts the force balance. For instance, the effect of gravity ceases whereas viscous and capillary forces dominate as CO2 accumulate below sealing layers [45] Capillary and buoyant forces have been shown to be dominate viscous forces for CO2 migration at the Utsira formation [13], and gives strong indications for expected flow dynamics and justification of modeling assumptions.

2.1.2 Petrophysical properties

In order to address how fluids flow in a reservoir system, it is essential to consider the unique properties of fluids. Density is an important property that is responsible for buoyant forces that dominate on the long term, an it dictates the vertical distribution of fluids at steady state. Hydrostatic instabilities initiates buoyant forces that displaces lighter fluids over heavier fluids.

Another important property is dynamic viscosity μ, a measure of a fluid's resistance to shear forces by movement of another fluid. Density and dynamic viscosity are generally not

6

fixed quantities, but are related to thermodynamic conditions through an equation of state [4]. Depending on the system under consideration, the equations can become quite complex, for instance if including phase mixing. In this work we assume phases remain distinct and do not account for mixing of components between phases. As a result, the equation of state simplifies significantly. The viscosity of a fluid contributes to the force balance by means of viscous forces, and thus effectively counteracts the gravity force inducing buoyant migration.

Fluids are also characterized by compressibility, describing the ability of an entity of fluid to change its volume subject to external forces. Compressibility is explicitly related to density by

$$c_f = \frac{1}{\rho} \frac{d\rho}{dp},$$

where c_f is the compressibility factor of the fluid. Generally, fluid compressibility depends on several factors including temperature, pressure and composition [39].

It is not only inherent properties of the fluids that dictate migration paths of CO2. The surrounding rock matrix greatly influences the potential for flow, which explains why well placement is a crucial factor for optimizing long-term CO2 storage. Permeability is a property describing the ability of a particular rock to transmit fluids. In the case of multiphase flow, each phase has an effective permeability describing its ability to flow by the presence of other phases. The absolute permeability $\boldsymbol{K}$ is the ability to transmit all fluids present in the pore space. If other phases are present, phase α will experience more resistance to flow than if it occupied the pore space alone. Thus, the effective permeability of a phase is always less than the absolute permeability, whose ratio is referred to as relative permeability $k_{r\alpha}$ and is bounded between zero and one. Whereas absolute permeability is an intrinsic property of the rock, relative permeability depends on the saturation of phase α in the pore space, usually as a nonlinear dependence.

Another essential property of the rock is porosity, expressing the fraction of rock volume consisting of pores for fluids to flow through. A lower porosity implies less volume to store and transmit fluids. To maximize injection capacity while keeping the pressure buildup at a minimum, it is vital to locate formations with high porosity. Generally, porosity is a pressure-dependent parameter, implying that rock is a compressible material with compressibility c_r defined as

$$c_r = \frac{1}{\phi} \frac{d\phi}{dp}.$$

2.1.3 Capillary pressure

In a multiphase system a fluid is subject to adhesive forces with the surrounding rock in addition to surface tension at the interface between the fluids present. The force balance is responsible for a pressure difference between the fluid known as capillary pressure. In a two-phase system, the capillary pressure is the pressure difference between a non-wetting phase n

and a wetting phase w in hydrostatic equilibrium, expressed as

$$p_c = p_n - p_w.$$

Depending on the dimensional scales of the system under consideration, capillary forces may have a significant impact on the distribution of phases, even in the context of geological CO2 storage [39]. Capillary pressure is often modeled through an inverse relationship of the saturation of the wetting phase, expressed as

$$P_c(S_w) = f^{-1}(S_w), \tag{1}$$

where f is assumed to be monotonic, in which case the expression can be inverted to obtain saturation S_w as a function of capillary pressure. When the capillary pressure is in equilibrium with the gravitational force, the transition zone between the wetting phase and non-wetting phase is a fully developed capillary fringe described by 1. Capillary pressure functions vary according to the wettability of the fluid phases and pore structure of the ambient rock. The capillary pressure determines to what extent a non-wetting fluid is able to displace a wetting fluid occuping some pore space, depending on if the entry pressure in this region is exceeded or not, where entry pressure is defined as the minimum pressure required for the non-wetting phase to displace the wetting phase. In the case of cylindrical pores, the entry pressure is expressed analytically through the Young-Laplace equation [39],

$$p_c = \frac{2\gamma \cos(\theta)}{r},$$

where γ is the surface tension between the two fluids and θ the contact angle between them. Tighter pore networks, i.e. pore throats with small radius r, give a larger capillary pressure. For long-term CO2 storage though, modeling is done on the reservoir scale that is too large to resolve pore size distribution on the microscale. Instead, it is customary to apply an averaged pore size so that the capillary pressure is essentially homogeneous within the rock matrix.

2.1.4 Residual saturation

Residual saturation is the saturation for which a fluid in some pore space becomes immobile. That is, as saturation decreases and reaches the residual saturation, the fluid goes from being mobile to becoming residually trapped by capillary forces in isolated pockets surrounded by ambient fluid.

Residual saturation influences the relative permeability curves. Instead of the relative permeability reaching zero at zero saturation, it reaches zero at the residual value. Moreover, if multiple phases are present in some pore space, the maximum relative permeability is not achieved for unit saturation but for one minus the residual saturation of the other phases. Because the Darcy

flux is a linear function of relative permeability, residual saturation has a significant effect on fluid migration.

Residual saturation is closely related to hysteretic behavior of fluids. As a nonwetting fluid enters new pore space, it displaces the current ambient wetting fluid in what is referred to as a displacement process. The relative permeability curve for primary displacement starts increasing at zero saturation. Once the wetting fluid imbibes the regions occupied by the nonwetting fluid, the relative permeability of the nonwetting fluid decreases until it reaches zero at the residual saturation. In other words, the particular relative permeability curve followed depends on the history of the system. For a two-phase system with wetting phase w and non-wetting phase n, the domain of non-wetting phase relative permeability for drainage and imbibition is given by, respectively,

$$D_{dr}(k_{rn}) \ : \ \{s_n \mid s_n \in [0, \ 1 - s_{wr}]\},$$
$$D_{im}(k_{rn}) \ : \ \{s_n \mid s_n \in [s_{nr}, \ 1 - s_{wr}]\}.$$

That is, during injection CO2 is mobile even for saturations below residual value. Relative permeability curves for a CO2 with residual saturation $s_{nr} = 0.15$ and $s_{wr} = 0.2$ including drainage and imbibition is shown in Figure 1.
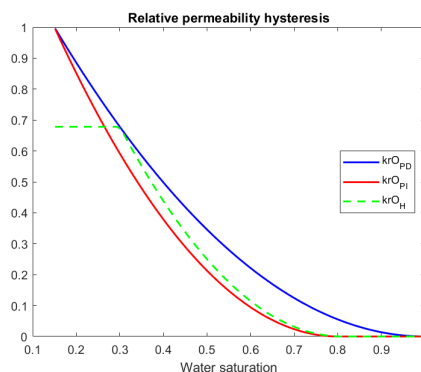
Figure 1: Relative permeability curves for CO2 for a hysteretic system with residual saturation. Blue curve is primary drainage curve, red curve is primary imbibition curve and green dashed curve shows imbibition curve for a reversal point $S_n > s_{nr} = 0.15$.

2.1.5 Governing equations

Darcy's law is an empirical relationship derived from the principle of conservation of momentum that describes flow through porous media. It states that the volumetric rate (flux) of a fluid through a pore system is proportional to the difference in hydraulic head $\delta h = \delta p/(\rho g) + \delta z$ at

two prescribed locations. The constant of proportionality depends on the permeability. In the case of multiphase flow, relative permeability becomes a factor and the multiphase extension of Darcy's law becomes

$$v_\alpha = -\frac{\mathbf{K}k_{r,\alpha}}{\mu_\alpha}(\nabla p_\alpha - \rho_\alpha \mathbf{g}), \tag{2}$$

where subscript α denotes a particular fluid phase and the vertical component is assumed to be positive downwards, as appropriate for a reservoir system. Vector and tensor quantities are represented in bold, and the distinction between them should be clear from context. For geological CO2 storage, 2 describes the fluxes of a two-phase system $\alpha = \{w, n\}$ where brine is the wetting phase w and CO2 is the non-wetting phase n.

The basic principle governing multiphase flow is conservation of mass with Darcy's law incorporated. The derivation is short and elegant. Consider an arbitrary closed volume Ω with boundaries denoted by $\partial\Omega$. To entail mass conservation we require that any change of mass M inside the volume is associated by a mass flux $\mathbf{f}$ into or out of the volume and external sources or sinks q. Accounting for contribution over the entire volume this becomes an integral expression,

$$\int_\Omega \frac{\partial M}{\partial t}\, dV = -\oint_{\partial\Omega} \mathbf{f} \cdot \mathbf{n}\, dA + \int_\Omega q\, dV.$$

The mass of the fluid per unit volume is given by $M = \rho\phi$ and the mass flux is $\mathbf{f} = \rho\mathbf{v}$, where $\mathbf{v}$ is the Darcy flux. By using Gauss' theorem, the surface integral can be transformed to a volume integral,

$$\int_\Omega \Big(\frac{\partial \rho\phi}{\partial t} + \nabla \cdot (\rho\mathbf{v}) - q\Big) dV = 0.$$

Based on the assumption that the volume Ω is arbitrary, it must be the case that the integrand itself is zero [39], which provides the equation of mass conservation for a single fluid

$$\frac{\partial(\rho\phi)}{\partial t} + \nabla \cdot (\rho\mathbf{v}) = q.$$

Multiple extensions exist depending on the system under consideration. Density of CO2 varies as a function of pressure and temperature, as described by equations of state, particularly near the critical point [39]. Thus, in the following derivation of the governing equations we account for fluid compressibility.

In the following derivation we assume that the fluids are compressible, and there is no mass transfer of components between phases. A multiphase extension yields one mass conservation equation per phase α, where the mass term is adjusted to account for pore space shared by multiple phases. Incorporating 2, the mass conserving equation for multiphase flow can be formulated as [28]

$$\frac{\partial}{\partial t}(\rho_\alpha \phi s_\alpha) + \nabla \cdot (\rho_\alpha \boldsymbol{u}_\alpha) = q_\alpha$$

$$\frac{\partial}{\partial t}(\rho_\alpha \phi s_\alpha) - \nabla \cdot (\rho_\alpha \frac{\boldsymbol{K}k_{r\alpha}}{\mu_\alpha}(\nabla p_\alpha - \rho_\alpha g \nabla z)) = q_\alpha, \tag{3}$$

where s_α and q_α are the saturation and source/sink term of phase α, $k_{r\alpha}$ and μ_α the relative permeability and viscosity of phase α, and $\boldsymbol{K}$ the intrinsic permeability of the rock.

The system 2 and 3 constitutes two equations but there are four unknowns, p_α and s_α for $\alpha = \{w, n\}$. To generate a closed system we need two additional closure equations. The first equation states that all available pore space is occupied the two phases, i.e.

$$s_w + s_n = 1.$$

The second one relates the difference in phase pressures to the capillary pressure curve, typically expressed in terms of water saturation

$$p_c(s_w) = p_n - p_w.$$

If the one phase pressure and one saturation is chosen as primary variables, the other phase pressure is obtained by the capillary pressure-saturation relation above.

Because the multiphase flow system consist of multiple equations with nonlinear dependencies, there are numerous ways to rewrite and solve them. A convenient method is to rewrite the system as an elliptic pressure equation a hyperbolic transport equation to decouple pressure and saturation. Thence, the pressure equation is not affected by the stability restrictions of the transport equation, allowing to use as large time step as desired for the former [28].

Applying the product rule on the first term in 3 gives [39]

$$\frac{\partial}{\partial t}(\rho_\alpha \phi s_\alpha) = \rho_\alpha \phi \frac{\partial s_\alpha}{\partial t} + s_\alpha \rho_\alpha c_{t,\alpha} \frac{\partial p_\alpha}{\partial t},$$

where $c_\alpha = c_\phi + \phi c_{f,\alpha}$ is the total compressibility. Plugging this into 3, dividing by ρ_α and summing over phases we end up with the following

$$\phi \sum_\alpha \frac{\partial s_\alpha}{\partial t} + \sum_\alpha s_\alpha c_{t,\alpha} \frac{\partial p_\alpha}{\partial t} - \sum_\alpha \frac{1}{\rho_\alpha} \nabla \cdot (\rho_\alpha \boldsymbol{u}_\alpha) = \sum_\alpha q_\alpha.$$

The first term evaluates to zero because $\frac{\partial}{\partial t}(s_w + s_n) = 0$ and we get the pressure equation

$$\sum_\alpha s_\alpha c_{t,\alpha} \frac{\partial p_\alpha}{\partial t} - \frac{1}{\rho_\alpha} \nabla \cdot (\rho_\alpha \boldsymbol{u}_\alpha) = \sum_\alpha q_\alpha, \tag{4}$$

to be solved for one of the phase pressures. By introducing the total Darcy velocity $\boldsymbol{u} = \boldsymbol{u_w} + \boldsymbol{u_n}$ and the fractional flow function $f_\alpha = \frac{\lambda_\alpha}{\lambda_w + \lambda_n}$, [28] shows how (3) can be developed to yield the transport equation

$$\frac{\partial}{\partial t}(\rho_w \phi s_w) + \nabla \cdot \left[\rho_w f_w \big(\boldsymbol{u} + \lambda_n \boldsymbol{K}(\Delta \rho g \nabla z + \nabla p_c \nabla s_w))\big)\right] = q_w \tag{5}$$

to be solved for the wetting phase saturation.

2.1.6 Trapping inventory

To address how much volume of CO2 has potential to leak, it is crucial to categorize the injected volumes by a trapping inventory. The free plume characterizes parts of injected CO2 that is mobile and has potential to leak. After water has reimbibed pore space occupied by CO2, a residual amount of CO2 will be left immobilized in the pores trapped by capillary forces. This quantity has become residually trapped and has no potential for leakage due to its immobility. Accumulated CO2 below impermeable layers is structurally trapped due to its inability to penetrate through the confining layer.

The free plume comprises the main concern within CO2 storage due to its leakage potential. Therefore, a central goal is to maximize amount residually trapped, obtained by maximizing the spread of CO2. Dissolution is a third trapping mechanism, describing the mass transport of components between phases. CO2 in gas phase can be permanently trapped by dissolving into the brine phase. The time-scale of which solubility becomes significant is sensitive to the reservoir system and may span several orders of magnitude [25]. In this thesis mixing of components between phases is not accounted for and solubility trapping is thus omitted. For the Sleipner field, dissolution has shown to be notable first after 100 years of migration, becoming the dominant trapping mechanism in late migration stage [2]. Our simulation results are thus expected to deviate significantly from other benchmark studies. The goal is not to reproduce realistic plume shapes, but rather compare hybrid models to expensive full-dimensional models for idealized scenarios.

Finally, dissolved CO2 can be immobilized by chemical interactions with brine and surrounding rock. The chemical processes involved are in many practical situations extremely slow and mineral trapping can safely be ignored in the models [43]. Among the four trapping mechanisms, structural trapping is the only one not providing inherent security. Residually trapped CO2 is effectively immobilized, while solubility and mineral trapping facilitate removal of a distinct CO2 phase either by dissolution in the brine phase, where the larger density of brine transfer dissolved CO2 downwards, or by precipitation into a solid, immobile by nature. Structural trapping mainly facilitate storage security on a short to intermediate time scale, residual and solubility trapping at an intermediate to long time scale and mineral trapping on a long time scale [32].

In contrast to residually trapped CO2, structurally trapped CO2 it is not trapped indefinitely as there might be imperfections and cracks in the sealing layer that eventually yields leakage. Hence, it is common to separate the structurally trapped CO2 in a residual part and a mobile part. Parts of the free plume outside structural traps can be separated into a mobile part whose fate is undetermined, and a residual part that is destined to be left immobilized and trapped indefinitely once brine reimbibes the pore space. At any time step during a simulation, it is customary to separate the injected CO2 into six categories, as exemplified in Figure 2, where the mass of CO2 reaches a constant value once injection ceases.
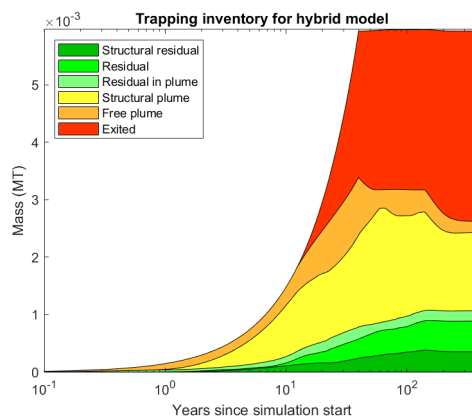

Figure 2: Example of a trapping inventory for a simulation with 40 years of injection and 400 years of migration, where mass of injected CO2 is separated into six categories.

To localize structural traps necessitates a technique called spill-point analysis. It is based solely on the geometry of sealing layers of the formation to compute spill locations, spill paths and downstream traps, hierarchically described by a spill-tree [4]. Unfortunately, the accuracy of the method is limited by grid resolution. If the grid cells are larger the wavelengths of local geometry oscillations, the associated local traps are not resolved. As a consequence, the analysis may predict erroneous spill points and spill paths that divert CO2 to other regions that are not apparent in the spill tree for the continuous setting [16]. It is important to be aware of this limitation when analysing a trapping inventory.

2.2 Dimensional scales

As briefly outlined in the introduction, the dimensional scales for CO2 storage simulation are large and span multiple orders of magnitude. The relative importance of the scales vary according to the specific problem. Accounting for the physics occurring at every relevant scale and combine them into a comprehensive numerical framework is extremely demanding. Therefore, it is essential to discern the most dominant scales and apply simplifications to other less influential

scales in order to make the computations manageable [14]. As the main focus of this thesis is simulation of long-term CO2 migration, we seek models tailored for the regional and basin scales. If the focus is rather to resolve local dynamics, i.e. in the vicinity of wells, other models adapted to the well scale are more appropriate [7]. In this section we briefly outline the governing scales for geological CO2 storage and present common simplifications.

2.2.1 Spatial scales

The spatial scales cover multiple orders of magnitude, characterized by different physical effects and contributions to the governing force balance. At the coarsest, one can distinguish between a microscopic scale, representing flow dynamics at the pore scale, and a macroscopic scale, representing flow between geological layers [39].

As for CO2 storage simulation, we are interested in long-term behavior at the macroscopic scale at which inertial forces dominate. Still, fluid flow at the pore scale influences dynamics at the macroscale. This is particularly true near wells and other regions characterized by large pressure gradients where viscous forces are dominant. In addition, capillary forces is a pore-scale phenomena that in many cases have a notable impact on the distribution of fluids at the macroscale and may ultimately prevent CO2 from penetrating a confining caprock [4]. At gravity-capillary equilibrium, the functional dependence between saturation and capillary pressure dictates the spatial extent of the transition zone between brine and CO2. If it is sufficiently small compared to the spatial scale of the formation, it can often be ignored and replaced by a sharp interface. Hence, the governing equations describe a system that is coupled through multiple spatial scales. To bridge the gap between the different scales, upscaling and multiscale modeling are essential components in long-term CO2 storage [39].

2.2.2 Temporal scales

The temporal scales of CO2 storage also span multiple orders of magnitude, and the distinction closely resembles that of the spatial scales. Their relevance depends on operational demands and the particular storage site. It is customary to identify five temporal scales, sorted from smallest to largest; the nano scale, micro scale, meso scale, macro scale and mega scale [39]. For long-term CO2 storage simulation considered in this thesis, physics at the nano and micro scales are much smaller than the long-term plume migration of interest and is omitted (i.e. considered to be in equilibrium). The meso scale defines the time used for fluids to segregate, which obviously depends on the storage site. Herein, we use numerical models based on the assumption that CO2 and brine are vertically segregated, except internally in low-permeable layers. Hence, the meso scale is generally of minor importance apart from calculation of fluxes in the vicinity of low-permeable regions. Our concern is mainly the injection phase represented by the macro scale, and the post-injection plume migration represented by the mega scale. Diffuse

leakage, very slow vertical migration of brine through almost impermeable layers induced by the overpressure from injected CO2 [4], is active on the mega scale, but induces changes to the pressure solution at the macro scale [39]. The macro and mega scales are the scales at which we want the governing equations to apply for. Thus, it is important to bridge the gap between these two scales, incorporating potentially important upscaled properties from the mesoscale.

2.2.3   Upscaling

Although accounting for pore-scale properties is inevitable for accurate simulation results, representing every pore numerically would require innumerable cells and is computationally infeasible. This challenge is inherently related to the characteristic scales outlined in the previous section. Effects at the finer scales are too small to be accounted for directly in a numerical model tailored for larger scales. Still it is possible to map fine-scale information to a coarser scale with the help of compression operators [39]. Generally, this is done by applying some sort of averaging of the properties. In practice, heterogeneities at the pore-scale are homogenized - or upscaled - to yield a single value representative at a larger scale. Vertical equilibrium models apply the principle of upscaling by merging vertically stacked layers into a single layer defined by upscaled variables with single unique value in the vertical. Permeability and porosity are rock properties defined for each grid block and need to be upscaled. To this end, standard averaging techniques are appropriate where the layers in the formation are either parallel or perpendicular to the pressure drop [28]. In a hybrid framework, upscaling is performed in parts of the domain that satisfy the VE assumption, where the main flow direction is in the vertical, perpendicular to the layering. Hence, harmonic average is the correct upscaling of permeability. Internally in low-permeable layers and close to wells, viscous forces dominate and the main flow direction is non-trivial, in which case arithmetic or harmonic averaging are not appropriate upscaling methods. However, since these regions are modeled as full-dimensional cells upscaling is not required.

There is also a desire to go the other way around, that is, retrieve fine-scale information from a coarse solution, both for computation of coarse-scale variables and for visualization purposes. Reconstructed fine-scale variables are obtained by applying reconstruction operators on coarse variables [39]. The appropriate operator depends on the assumptions behind the model. For particularly simple problems the operator may be a closed-form expression, for instance in a sharp interface model that will be discussed later in this thesis. In general though, reconstruction is non-trivial and will require numerical integration and non-linear calculations [39].

Generally, upscaling properties is not trivial. Different methods for averaging a property yield different simulation results in terms of accuracy. Absolute permeability is a tensorial quantity that complicates the search of an optimal upscaling method. Despite the challenges, multiscale methods are an inevitable part of reservoir simulation to obtain a continuum description linking

pore-scale behavior to the macroscale governing equations [29]. Discussion of appropriate up-scaling techniques is beyond the scope of this thesis. For more details, please consult chapter 15 of [28].

3 Numerical methods

The multiphase flow equations presented in 2.1.5 include explicit and implicit nonlinear dependencies and are strongly coupled, leading to a system that is difficult to solve. Analytical solutions exists only for particularly simple problems involving homogenized reservoir properties and limited spatial and temporal scales [39]. In general though, the governing equations for long-term migration of CO2 are too complex and one have to rely on numerical computations to solve the two-phase flow system. The goal of numerical methods is to compute approximate and reliable solutions of the true continuous system within a reasonable time.

The governing equations presented in Physical description: governing equations represent the state of the multiphase flow system in a continuous setting. A computer is not able to render the concept of a derivative necessary to describe how the continuous system evolves in time. Instead one must rely on a discrete representation of the system by discretizing the reservoir into a finite number of cells and faces that collectively represent the computational domain. The governing equations must correspondingly be converted to a discrete complement that can be solved numerically as an approximation to the continuous counterpart.

To this end, the Matlab Reservoir Simulation Toolbox (MRST) - an open-source software for reservoir simulations [37] - is used to develop the models studied in this thesis. This includes the full computational pipeline from grid setup, equation discretization, numerical solvers and a wide range of visualization options of the results. The core of MRST is an object-oriented framework that utilizes automatic differentiation to efficiently calculate derivatives to machine precision.

Choice of numerical methods to discretize a set of partial differential equations is not trivial. Depending on the equation system, the methods differ by convergence, stability and computational efficiency and the tradeoff among these is an important consideration [27].

3.1 Two-point flux approximation

To derive a discretized version of the governing multiphase flow equations to be solved numerically, the physical properties need to take on discrete values in the spatial dimensions that constitute the computational domain. The principle of mass conservation governing the continuous system must also hold in a discrete sense. Finite difference methods are mathematically simple to implement, but are restricted to regular geometry and mass conservation is only valid when the spatial resolution goes to zero [3]. To facilitate unstructured grids and conserve mass, it is appropriate to use a finite-volume method to discretize space, more specifically the widely used two-point flux approximation (TPFA) for multiphase systems that is based on conservation of mass over cells accompanied by continuity of fluxes across faces [28] and is illustrated in Figure 3. The derivation herein is based on a two-phase flow system of a liquid and a gas, as relevant for CO2 storage simulation.
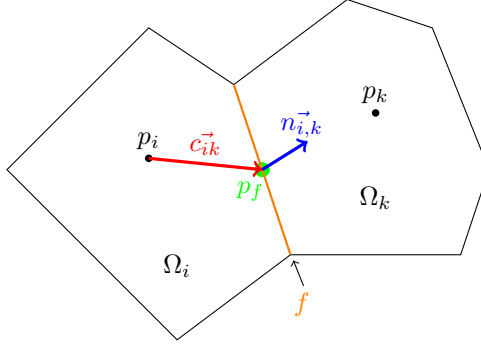
Figure 3: Sketch of flux of phase α across an interface $f = \Gamma_{i,k}$ shared by two cells Ω_i and Ω_k used to derive the Two-Point Flux Approximation (TPFA).

Consider the second term in 3. This includes the divergence of the flux function, defined over cells, as opposed to the phase flux itself defined over faces. The TPFA scheme used to discretize the phase fluxes is thus essentially a mapping from faces to cells. To this end, we assume incompressible fluids and consider the pressure equation 4 now simplified to

$$
\begin{aligned}
\nabla \cdot \mathbf{u}_\alpha &= q_\alpha, \\
\mathbf{u}_\alpha &= -\frac{\mathbf{K} k_{r\alpha}}{\mu_\alpha}(\nabla p_\alpha - \rho_\alpha g \nabla z).
\end{aligned}
\tag{6}
$$

Integrating over cell volume Ω_i and applying the divergence theorem gives

$$
\int_{\partial\Omega_i} \mathbf{u}_\alpha \cdot \mathbf{n}\, dS = \int_{\Omega_i} q_\alpha\, dV.
$$

The net flux from cell i to cell k across the interface $f = \Gamma_{i,k}$ with normal vector $\mathbf{n}_{i,k}$ and area $A_{i,k}$ is given by

$$
\mathbf{u}_\alpha^{i,k} = \int_{\Gamma_{i,k}} \mathbf{u}_\alpha \cdot \mathbf{n}\, dS.
$$

Assuming the interfaces between cells are continuous, each half-face has a complement with same face area $A_{k,i} = A_{i,k}$ but opposite normal vector $\mathbf{n}_{k,i} = -\mathbf{n}_{i,k}$. Evaluating the flux at the centroid, $x_{i,k}$, of f, using the midpoint rule, we have

$$
u_\alpha^{i,k} = A_{i,k}\mathbf{u}_\alpha(x_{i,k}) \cdot \mathbf{n}_{i,k} = -A_{i,k}\frac{\mathbf{K} k_{r\alpha,f}}{\mu_\alpha}(\nabla p_\alpha - \rho_\alpha g \nabla z)|_{x_{i,k}} \cdot \mathbf{n}_{i,k},
$$

where $u_\alpha^{i,k}$ is the volumetric flux directed from cell i to cell k.

Assuming the pressure at the center of cell i equals the cell-averaged pressure $p_{\alpha,i}$, and the pressure at the center of face f is $p_{\alpha,f}$, the pressure gradient can be approximated as $\nabla p_\alpha =$

$p_{\alpha,f} - p_{\alpha,i}$. Thence, the flux from cell i across f becomes

$$
\begin{aligned}
u_\alpha^{i,k} &= -A_{i,k} \frac{\mathbf{K} k_{r\alpha,f}}{\mu_\alpha} \frac{\big((p_{\alpha,f} - p_{\alpha,i}) - \rho_\alpha g(z_f - z_i)\big) \mathbf{c}_{ik}}{|\mathbf{c}_{ik}|^2} \cdot \mathbf{n}_{i,k} \\
&= T_{i,k} \lambda_{\alpha,f} \big((p_{\alpha,i} - p_{\alpha,f}) - \rho_\alpha g(z_i - z_f)\big).
\end{aligned}
\tag{7}
$$

where $\lambda_{\alpha,f} = k_{r\alpha,f}/\mu_\alpha$, $\mathbf{c}_{i,k}$ is the vector pointing from the centroid of cell i to $x_{i,k}$ and $T_{i,k}$ is the half-face transmissibility for the half-face $\Gamma_{i,k}$. The transmissibility is solely described by the cell geometry and the permeability of the rock and is therefore independent of phases α present.

Pressures are by default evaluated for cells, but the flux is evaluated at faces. Fortunately, the face pressure $p_{\alpha,f}$ can be eliminated by addressing the one-sided flux from the other side of the interface f in direction $\mathbf{n}_{k,i} = -\mathbf{n}_{i,k}$,

$$
u_\alpha^{k,i} = T_{k,i} \lambda_{\alpha,f} \big((p_{\alpha,k} - p_{\alpha,f})) - \rho_\alpha g(z_k - z_f)\big)
$$

To conserve mass, the one-sided fluxes across an interface must be equal but opposite directed, $u_\alpha^{i,k} = -u_\alpha^{k,i} = u_\alpha^f$. Combining the expressions for the one-sided fluxes, $p_{\alpha,f}$ can be eliminated, and we arrive at the TPFA scheme giving the net flux across a face bounded by cells i and k,

$$
\begin{aligned}
u_\alpha^f &= (T_{i,k}^{-1} + T_{k,i}^{-1})^{-1} \lambda_{\alpha,f} \big((p_{\alpha,i} - p_{\alpha,k}) - \rho_\alpha g(z_i - z_k)\big) \\
&= T_{ik} \lambda_{\alpha,f} (\nabla p_\alpha - \rho_\alpha g \nabla z)_{ik},
\end{aligned}
\tag{8}
$$

where T_{ik} is the face transmissibility given as the harmonic average of the half-face transmissibilities $T_{i,k}$ and $T_{k,i}$.

The benefit of using the TPFA scheme is that it is simple to implement, robust for structured grids and strictly monotone if transmissibilities are nonzero [28]. On the other hand, the scheme is infamous for producing grid orientation effects for anisotropic permeability and unstructured grids not aligned in the principal directions of the permeability tensor (non-K-orthogonal grids), customary features for real formation with faults. To obtain a more accurate solution for these petrophysical settings and grid geometries one generally has to rely on more advanced methods such as MPFA-O or mimetic methods [28], [29].

3.2   Single-point upwinding

Just like the TPFA scheme uses the harmonic average to evaluate the transmissibility at an interface between two cells, phase saturations are also cell-wise properties that need to be evaluated for faces to yield well-defined phase mobility $\lambda_{\alpha,f}$ over face f. From the discussion of upscaled permeability, it is tempting to use the harmonic average to upscale phase mobilities.

However, this will effectively immobilize a phase if one of a pair of neighboring cells has zero phase saturation [39]. Saturation is a property transported with finite speed by the hyperbolic flux term of 3 that rather suggests that mobilities are upstream weighted [12]. The single-point upwind scheme works by choosing the saturation from the upwind cell, i.e. the cell for which the flux across the face originates from, mathematically,

$$
\lambda_{\alpha,f} = \begin{cases} \lambda_{\alpha,f}(s_{\alpha,i}) & \Theta_{\alpha,i} > \Theta_{\alpha,k}, \\ \lambda_{\alpha,f}(s_{\alpha,k}) & \Theta_{\alpha,i} < \Theta_{\alpha,k}, \end{cases}
$$

where $\Theta_\alpha = p_\alpha - \rho_\alpha g z$ is the phase potential. Upwinding is simple to implement and has been proven to converge to the correct solution [12]. However, if the flux functions are not self-sharpening, the SPU-scheme suffers from numerical diffusion and better alternatives for the upwind operator are high-resolution discontinuous Galerkin methods and WENO discretization [29].

3.3 Discrete DIV, GRAD and UPW operators

To complete the spatial discretization of the multiphase flow system, we need discrete versions of the divergence, gradient and upwind operators. The definition of these operators depend on grid topology. This has the benefit that the discretized equation system closely resembles the continuous counterpart and generalizes the TPFA scheme [28] for more complex problems.

In 8, the gradient operator was encapsulated in the term $\Theta_{\alpha,i} - \Theta_{\alpha,k} = (p_{\alpha,i} - p_{\alpha,k}) - \rho_\alpha g(z_i - z_k)$. The continuous gradient operator evaluates changes in a property across a finite distance. The discrete version is formulated as the difference between two neighboring cell properties evaluated at the interface between them. In other words, the discrete GRAD maps from cells to faces. Let C denote the set of cells, F the set of faces, $\mathcal{R}^C$ the dimension for cells and $\mathcal{R}^F$ the dimension for faces. Then we have that the discrete gradient GRAD : $\mathcal{R}^C \to \mathcal{R}^F$ for a vector of scalar functions $\boldsymbol{p} \in \mathcal{R}^C$ is given by

$$
\texttt{GRAD}(\boldsymbol{p})[f] = \boldsymbol{p}(c_d(f)) - \boldsymbol{p}(c_u(f)), \tag{9}
$$

where c_d and c_u are the downstream and upstream cells for face f, respectively.

The discrete divergence operator should map from faces to cells to make the face-evaluated Darcy fluxes $\boldsymbol{u}_\alpha$ consistent with the cell-evaluated conservation equation 3. Hence, we have that GRAD : $\mathcal{R}^F \to \mathcal{R}^C$ for a vector field $\boldsymbol{v} \in \mathcal{R}^F$ is given by

$$
\texttt{DIV}(\mathbf{v})[c] = \sum_{f \in F(c)} \mathbf{v}[f]\mathbf{I}(c = c_d) - \sum_{f \in F(c)} \mathbf{v}[f]\mathbf{I}(c = c_u), \tag{10}
$$

where element c of vector $\mathbf{I}(c = c_d)$ or $\mathbf{I}(c = c_u)$ evaluates to one if c is downstream neighbor or

upstream neighbor to face f, respectively.

The discrete version of the upwind operator maps from cells to faces and is given by

$$\text{UPW}(\boldsymbol{x}, \Theta)_{ik} = \begin{cases} x_i, & \Theta_{ik} < 0, \\ x_k & \Theta_{ik} > 0, \end{cases} \tag{11}$$

where $\Theta_{ik} = (p_k - p_i) - \rho g(z_k - z_i)$ is the phase potential for cell i and k.

3.4 Fully-implicit equation system

With the transport of phase properties accounted for, and discrete versions of gradient, divergence and upwind operators, the TPFA scheme with single-point upwinding (TPFA-SPU) is generalized to

$$\begin{aligned} \text{DIV}(\boldsymbol{u}_\alpha)_{ik} &= q_\alpha \\ \boldsymbol{u}_{\alpha,ik} &= -\text{UPW}(\lambda_\alpha, \Theta_\alpha)_{ik} T_{ik} \Theta_{\alpha,ik} \\ \Theta_{\alpha,ik} &= \text{GRAD}(p)_{ik} - \bar{\rho}_{\alpha,ik} g \text{GRAD}(z)_{ik}, \end{aligned} \tag{12}$$

where $\bar{\rho}_{\alpha,ik}$ is the arithmetic average of phase density over cells i and k, which themselves depend on the cell pressures p_i and p_k for compressible fluids.

To complete the numerical scheme, the remaining terms in 3 need to be discretized. This necessitates a discretization in time, for which we choose a fully-implicit approach. The idea is to approximate the unknown variables at the next time step. Combined with the discrete spatial operators, the two-phase flow system is discretized compactly as

$$\frac{(\rho_\alpha \phi s_\alpha)^{n+1} - (\rho_\alpha \phi s_\alpha)^n}{t^{n+1} - t^n} + \text{DIV}(\rho_\alpha \boldsymbol{u}_\alpha)^{n+1} = q_\alpha^{n+1}, \tag{13}$$

with $\boldsymbol{u}_\alpha$ as given in 12. In MRST, the AD-OO framework combined with the flexibility of state functions provides a practical way to change the definition of the discrete operators DIV, GRAD and UPW without modifying the governing equation system [29].

The nonlinear nature and strong coupling facilitates numerous possible rearrangements of the multiphase flow equations, which again allows for multiple numerical strategies [39]. Using the formulation with a pressure and transport equation, a sequential solution strategy can be adopted where the pressure equation is first solved implicitly in time for the pressure and the thereafter the transport equation is solved explicitly for the saturation. Hence, the method is referred to as Implicit Pressure Explicit Saturation (IMPES). Unfortunately, for long-term CO2 storage problems, the effect of gravity at the sharp interface between CO2 and brine appears as a second-order term that amplifies the parabolic character of the transport equation, which usually yields a too strong coupling between the pressure and transport equations for the IM-

PES method to produce satisfactory results [39], [24]. Moreover, the IMPES method is generally not robust for systems approaching steady state and if saturations change significantly during a time step, as is customary for long-term CO2 storage [23], [11]. The fully implicit scheme, on the other hand, is unconditionally stable for arbitrary time step selection, but generally requires heavier computations than the IMPES method. Implementation-wise, the fully-implicit scheme is more convenient in the sense that the original formulation retains when including additional physical effects [24], for instance residual saturation, capillary pressure and compressibility, as will be accounted for in this thesis. Despite the stability of the scheme, longer time steps induce larger errors and requires more iterations to converge.

3.5 Newton's method

The solution vector $\boldsymbol{x}^{n+1}$ for time step $n+1$ in the fully-implicit scheme is generally a nonlinear expression that cannot be solved for analytically. This is particularly true for multiphase systems where additional nonlinear dependencies arise in the relative permeability and capillary pressure functions. The solution vector must be solved for numerically by an iterative procedure. A frequently used approach is Newton's method that possesses quadratic convergence given that the initial solution guess $\boldsymbol{x_0}^{n+1}$ is sufficiently close to the true solution. The method iteratively finds better approximations to the zeros of a function $\boldsymbol{F}(\boldsymbol{x}_{k+1})$ by a linear Taylor expansion around the current best guess $\boldsymbol{x}_k$ of the solution. Let the abstract form of the equation system at time step $n+1$ be written as $\boldsymbol{F}(\boldsymbol{x}^{n+1}, \boldsymbol{x}^n) = 0$, where $\boldsymbol{x}^{n+1} = [\boldsymbol{p}^{n+1}, \boldsymbol{s}^{n+1}]$ is the vector of primary unknowns, chosen as the water pressures $\boldsymbol{p}^{n+1} = \boldsymbol{p}_w^{n+1}$ and the gas saturations $\boldsymbol{s}^{n+1} = \boldsymbol{s}_g^{n+1}$ for a liquid-gas system considered herein. A first order Taylor expansion of $\boldsymbol{F}$ around the solution guess $\boldsymbol{x}_k^{n+1}$ gives

$$\hat{\boldsymbol{F}}(\boldsymbol{x}_{k+1}^{n+1}) = \boldsymbol{F}(\boldsymbol{x}_k^{n+1}) + \boldsymbol{J}(\boldsymbol{x}_k^{n+1})(\boldsymbol{x}_{k+1}^{n+1} - \boldsymbol{x}_k^{n+1}) = 0.$$

A Newton iteration k for $k \in [0, K]$, where K is the imposed maximum number of iterations, at time step $n+1$ is given by

$$\boldsymbol{x}_{k+1}^{n+1} = \boldsymbol{x}_k^{n+1} - \omega \frac{\boldsymbol{F}(\boldsymbol{x}_k^{n+1}, \boldsymbol{x}_k^n)}{\boldsymbol{J}(\boldsymbol{x}_k^{n+1})}, \tag{14}$$

where $\omega \in [0, 1]$ is a relaxation parameter that controls the step size we take in the direction of the true solution and may facilitate convergence by avoiding overshooting [31]. For long-term CO2 storage simulations where long time intervals are customary, the solution procedure is sensitive to overshooting. Thus, despite increased simulation time, it is vital to ensure that the number of iterations K is sufficiently high and the relaxation ω sufficiently small to obtain a reliable solution.

3.6 Trap analysis

In order to generate a trapping inventory we need to find all regions that fulfill the requirements of structural traps. This is done by a first-order geometrical and topological analysis of the top surface of a formation, for which traps, spill points and spill paths are calculated [40], [35]. For an exposition of how a trap analysis is conducted, please consult [4]. There are more computations in a hybrid framework due to the presence of multiple semi-permeable layers, but the calculations follow the same principle. That is, we extract the top surface of multiple subgrids, each bounded by a semi-permeable layer, and perform separate trap analysis for each of them. The top surfaces are mutually exclusive, facilitating a parallelized trap analysis. Extraction of top surface subgrids for a multilayered system is shown in Figure ?? (MISSING FIGURE!). Notice that the subgrids do not overlap and that "empty" regions are imposed fine cells whose CO2 mass distribution is calculated from cell-wise saturations, i.e. no trap analysis. In this thesis, *semi-permeable layers* are treated to have sufficiently low permeability and entry pressure to be considered as structural traps in the trapping inventory, unless stated otherwise. This is a reasonable statement considering the fact that CO2 is not trapped in indefinitely, but may leak through cracks and imperfections in the semi-permeable layers [24].

4 Vertical equilibrium models

The combination of large spatial and temporal scales imposes a computational expense that is without doubt the biggest challenge for simulating geological CO2 storage. As such, there is an aspiration for developing simplified models that reduce the computational cost while minimizing loss in accuracy. Analytical and semi-analytical models have been developed the last decade in addition to conventional 3D reservoir simulators that are computationally very expensive for long-term simulation. The former is unfortunately only applicable for highly idealized scenarios [39]. One generally has to rely on numerical methods, for instance for multilayered heterogeneous formations such as Utsira. Even so, for particular problems where viscous forces are negligible compared to gravity and capillarity, it is justified to reduce the vertical dimension, an assumption referred to as vertical equilibrium.

Vertical equilibrium models significantly reduce the computational complexity while retaining as much as possible of the conventional black-oil formulation [41]. It is based on the assumption that the reservoir fluids are rapidly segregated vertically after an initial distribution. This assumption is justified in regions where the fluids are subject to predominant buoyant forces caused by large density differences [8]. In a typical CO2 storage scenario the lateral scales are much larger than the vertical scales, implying that in the long term lateral flow will dominate vertical flow. Combined with significant density differences between CO2 and brine, even in supercritical state [32], the segregation process can in many cases be assumed to happen instantaneously, at least compared to the time-scale of lateral up-dip migration [24]. Thus, the fluids are in hydrostatic equilibrium and the vertical dimension is redundant. The vertical dimension is effectively removed by integrating the flow equations vertically between the bottom and top of the formation. Therefore, the vertical equilibrium models are based on a set of upscaled variables that only depend on lateral dimensions since the vertical dimension has been "integrated away". Vertical pressure and saturation are trivial to reconstruct analytically from the hydrostatic assumption.

Because the vertical equilibrium columns are agglomerations of fine-scale cells, petrophysical and geometric fine-scale properties including absolute permeability, porosity and transmissibility need to be averaged on the coarse scale by an upscaling technique [28]. Section 2.2.3 justified that harmonic averaging of absolute permeability $\boldsymbol{K}$ is the correct upscaling technique for VE cells. If b, t and H defines the bottom, top and thickness of the VE column, respectively, and $\boldsymbol{x}$ the location of fine-scale cells, the harmonic average of $\mathbf{K}$ is given by

$$\bar{\boldsymbol{K}} = \Big(\frac{1}{H} \int_b^t \frac{1}{\mathbf{K}(\boldsymbol{x})} \, d\vec{x} \Big)^{-1}.$$

The discretized harmonic average used in the numerical solver for a VE column made up of n fine cells of thicknesses h_i is

$$\bar{\boldsymbol{K}} = \Big(\frac{1}{\sum_{i=1}^n h_i} \sum_{i=1}^n h_i \frac{1}{\mathbf{K_i}} \Big)^{-1}.$$

Assuming uniform spacing between the fine cells in the vertical direction, $h_i = H/n$ and the harmonic average simplifies to

$$\bar{K} = \frac{n}{\sum_{i=1}^{n} \frac{1}{K_i}}.$$

Notice that for aquifers where permeability is homogeneous (constant) in the vertical direction, arithmetic average and harmonic average give the same upscaled permeability, i.e. $\bar{K} = K_i = K$, even for nonuniform grid spacing.

Porosity is a volumetric quantity that is upscaled simply by adding up pore volumes from fine cells with volume V_i and normalizing by total pore volume in the VE column. The discretized average is

$$\bar{\phi} = \frac{1}{\sum_{i=1}^{n} V_i} \sum_{i=1}^{n} V_i \phi_i.$$

Because the face areas of cells are incorporated in the definition of transmissibility, the upscaled transmissibility of a VE column is obtained by summation over m fine-scale transmissibilities for faces bounding the VE column, without scaling by formation thickness,

$$\bar{T} = \sum_{i=1}^{m} T_i,$$

where it is implicitly assumed that the fine-scale face transmissibilities T_i are computed as a harmonic average of associated half-faces

$$T_i = \left(\frac{1}{T_{i,d}} + \frac{1}{T_{i,u}} \right),$$

where $T_{i,d}$ is the half-face transmissibility for face i from downstream cell d and $T_{i,u}$ half-face transmissibility from upstream cell u.

In the VE assumption fluid phases are in hydrostatic equilibrium which implies that the vertical pressure distribution follows a hydrostatic profile dictated by the weight of the overlying column of fluid. The hydrostatic pressure distribution for phase α in an aquifer with slope angle θ is given by

$$p_\alpha = P_\alpha + \rho_\alpha g(z - z_0) \cos(\theta), \tag{15}$$

where P_α is the pressure at a prescribed depth z_0.

The VE model is obtained by vertically integrating the multiphase flow extension of the mass conserving equation. Retaining generality, we let x_1 and x_2 denote the coordinates in the lateral direction of the aquifer and z the coordinate transversal to the aquifer. Hence, for a sloped aquifer, z will deviate slightly from the true vertical, but we will herein label it as the vertical direction regardless. A sketch of the system under consideration is shown in Figure 4. Consistent with section 2.1.5, we model compressible fluids. The vertical integrated version of 3 is
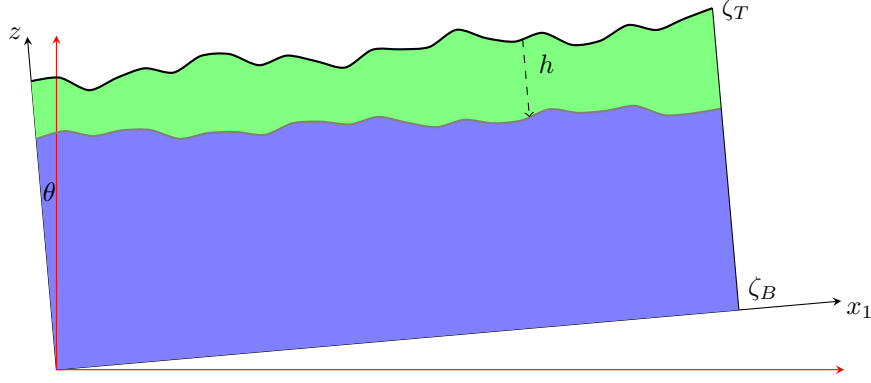
Figure 4: Sketch of a reservoir system used to derive the basic sharp interface vertical equilibrium model. Red axes represent the main coordinate frame, while black axes represent the coordinate used in the derivation, rotated by an angle θ. The system is only shown in 2D as we assume the cross-section is uniformly extruded in the x_2-direction.

$$\int_{\zeta_T}^{\zeta_B} \frac{\partial}{\partial t}\left(\rho_\alpha s_\alpha \phi\right) dz - \int_{\zeta_T}^{\zeta_B} \nabla \cdot \left[\rho_\alpha \frac{k_{r,\alpha}\mathbf{K}}{\mu_\alpha}(\nabla p_\alpha - \rho_\alpha \mathbf{g})\right] dz = \int_{\zeta_T}^{\zeta_B} q_\alpha \, dz$$

Under the assumption of no flow across top and bottom boundaries, Leibniz' rule can be used to move the divergence outside the integral. Assuming the rock properties in the principal directions are independent of each other, the permeability can be decomposed into a lateral component (denoted $\parallel$) and a transversal component (denoted $\perp$),

$$\mathbf{K} = \mathbf{K}_\parallel \mathbf{K}_\perp.$$

Consequently, the Darcy flux can be decomposed and lateral flow will only depend on the lateral pressure gradient [4], in which case the vertical component vanishes and we get

$$\frac{\partial}{\partial t}\int_{\zeta_T}^{\zeta_B} \left(\rho_\alpha s_\alpha \phi\right) dz - \nabla_\parallel \cdot \int_{\zeta_T}^{\zeta_B} \rho_\alpha \lambda_\alpha \mathbf{K}_\parallel (\nabla_\parallel p_\alpha - \rho_\alpha \mathbf{g}_\parallel) \, dz = \int_{\zeta_T}^{\zeta_B} q_\alpha \, dz \tag{16}$$

For compressible fluids, the phase densities are not only functions of depth z and reference scalars P_α and ζ_T, but also on temperature T. Hence, an extended variant of 15 leads to the following lateral pressure gradient given as a total differential [5]

$$\nabla_\parallel p_\alpha = \frac{\partial p_\alpha}{\partial P_\alpha}\nabla_\parallel P_\alpha + \cos(\theta)\frac{\partial p_\alpha}{\partial \zeta_T}\nabla_\parallel \zeta_T + \frac{\partial p_\alpha}{\partial T}\mathbf{g}_\parallel$$

$$= \nu_{p,\alpha}\nabla_\parallel P_\alpha + \cos(\theta)\nu_{\zeta,\alpha}\nabla_\parallel \zeta_T + \nu_{g,\alpha}\mathbf{g}_\parallel$$

The coefficients ν_p, ν_ζ and ν_g define a system of ODEs that can be solved and shown to give

the following integrated version of 3

$$\frac{\partial}{\partial t} \int_{\zeta_T}^{\zeta_B} (\rho_\alpha s_\alpha \phi)\, dz - \nabla_\parallel \cdot \int_{\zeta_T}^{\zeta_B} \rho_\alpha \mathbf{K}_\parallel \lambda_\alpha \nu_{p,\alpha} \big(\nabla_\parallel P_\alpha - \rho_\alpha (g_\perp \cos(\theta)\nabla_\parallel \zeta_T + \boldsymbol{g}_\parallel)\big)\, dz = \int_{\zeta_T}^{\zeta_B} q_\alpha\, dz$$

The lateral components of the pressure gradient and gravity are independent of the transversal direction, yielding

$$\frac{\partial}{\partial t} \int_{\zeta_T}^{\zeta_B} (\rho_\alpha s_\alpha \phi)\, dz - \nabla_\parallel \cdot \Big[\int_{\zeta_T}^{\zeta_B} \rho_\alpha \mathbf{K}_\parallel \lambda_\alpha \nu_{p,\alpha}\, dz \Big] \big(\nabla_\parallel P_\alpha - \rho_\alpha (g_\perp \cos(\theta)\nabla_\parallel \zeta_T + \boldsymbol{g}_\parallel)\big)\, dz = \int_{\zeta_T}^{\zeta_B} q_\alpha\, dz \tag{17}$$

Next, we define the following upscaled variables

$$\Phi = \int_{\zeta_T}^{\zeta_B} \phi\, dz$$

$$S_\alpha = \Phi^{-1} \int_{\zeta_T}^{\zeta_B} \phi s_\alpha\, dz$$

$$R_\alpha = \Phi^{-1} S_\alpha^{-1} \int_{\zeta_T}^{\zeta_B} \rho_\alpha \phi s_\alpha\, dz$$

$$\boldsymbol{\kappa} = \int_{\zeta_T}^{\zeta_B} \mathbf{K}_\parallel\, dz$$

$$\boldsymbol{\Lambda}_\alpha = \boldsymbol{\kappa}^{-1} \int_{\zeta_T}^{\zeta_B} \frac{k_{r\alpha}}{\mu_\alpha} \mathbf{K}_\parallel\, dz$$

$$\hat{\boldsymbol{R}}_\alpha = \boldsymbol{\kappa}^{-1} \boldsymbol{\Lambda}_\alpha^{-1} \int_{\zeta_T}^{\zeta_B} \rho_\alpha \lambda_\alpha \mathbf{K}_\parallel\, dz$$

$$\boldsymbol{N}_\alpha = \hat{\boldsymbol{R}}_\alpha^{-1} \boldsymbol{\kappa}^{-1} \boldsymbol{\Lambda}_\alpha^{-1} \int_{\zeta_T}^{\zeta_B} \nu_{p,\alpha} \rho_\alpha \lambda_\alpha \mathbf{K}_\parallel\, dz$$

$$Q_\alpha = \int_{\zeta_T}^{\zeta_B} q_\alpha\, dz,$$

which produces the following upscaled form of the governing multiphase flow equations

$$\frac{\partial}{\partial t}(R_\alpha \Phi S_\alpha) + \nabla_\parallel \cdot \boldsymbol{F}_\alpha = Q_\alpha \tag{18}$$

$$\boldsymbol{F}_\alpha = -\boldsymbol{N}_\alpha \hat{\boldsymbol{R}}_\alpha \boldsymbol{\Lambda}_\alpha \boldsymbol{\kappa} \big(\nabla_\parallel P_\alpha - \rho_\alpha (g_\perp \cos(\theta)\nabla_\parallel \zeta_T + \boldsymbol{g}_\parallel)\big)$$

All upscaled quantities, except phase pressures, are based on vertical integration over the aquifer thickness to remove the dependence on the vertical coordinate. Upscaled phase pressures are instead sampled at a reference depth since vertical averaging of pressure is not a physical

meaningful variable [6].

The final set of equations has been reduced from three dimensions to two and has the same structural form as the original fine-scale equations. Hence, the numerical solution strategy is principally the same as for the fine-scale complement, in which case the implementation is straightforward as long as the upscaled variables have analytical expressions [39]. In the more general case, numerical integration or tabulation is needed to derive the upscaled quantities before the equation system can be solved [23].

A question to ask is when the VE assumption is valid. A qualitative measure from [20] suggests the following segregation time for fluid phases

$$t_s \sim \frac{H \phi \mu_w}{k_{rw} k_z \Delta \rho g},$$
(19)

where H is the aquifer thickness, μ_w the viscosity of brine, k_{rw} the relative permeability of brine and k_z the vertical permeability of the layer. If t_s is much less than the simulation time T, $t_s << T$, vertical equilibrium is a reasonable approximation. Applying this on the Utsira formation, we can ascertain that the VE assumption holds for most parts of the formation due to predominant sandstone layers with high k_z. The same holds for $\Delta \rho$ as already elaborated. Moreover, since layers of sandstone are separated by thin layers of shale, the heights H of individual sandstone layers are small compared to formation thickness [13]. Hence, time of segregation in the high-permeable sandstone layers is very small compared to a long-term injection-migration scenario. Applying the same expression for the layers of shale, it is clear that segregation times are significantly longer and VE is not a justified approximation here.

Despite a reduction in dimensionality, the VE model is not destined to yield worse results than the full-dimensional model in regions where the VE assumption applies. In fact, a VE model may give a better solution in these regions than a full-dimensional model because the former is not limited by a finite grid resolution in the vertical direction, but rather relies on analytical reconstruction [34], [30]. Because the governing coarse equations are principally derived in the same way as the full-dimensional equations, the principle of mass conservation still applies for the coarse variables, thus equation 18 satisfies a conservation law in the new solution space [39] with a physical interpretation. The fact that the coarse-scale variables depends on the fine-scale variables induces some challenges, as the fine-scale variables somehow need to be estimated. An obvious approach is to solve the fine-scale system of equations, but this is computationally expensive and exactly what we are trying to avoid. Instead, the fine-scale variables can be approximated through reconstruction operations [39]. This will usually involve evaluation of nonlinear equations [23], but for particularly simple problems the reconstructions have simple analytical expressions. This will be outlined in a later section.

4.1 Reconstruction

The solution of the upscaled system of equations represents a two-dimensional surface at the reference depth used for upscaling. Visualizing a 2D surface is of limited value as we lose information of the interior of the formation. Fortunately, fine-scale variables representing the three-dimensional solution can be reconstructed from the coarse-scale variables using the vertical equilibrium assumption [39]. More importantly than for visualization purposes, the reconstructed variables are an inevitable part of the equation system since they are used to evaluate upscaled quantities.

Let P_α denote the upscaled pressure for phase α at a reference depth, herein chosen to be the top surface of an aquifer plane with dip angle θ. The fine-scale pressure is reconstructed by knowledge of the depth of the top surface ζ_T and the weight of the overlying column of fluid,

$$p_\alpha(x, y, z) = P_\alpha(x, y) + \rho_\alpha g\big(z - \zeta_T(x, y)\big) \cos(\theta). \tag{20}$$

As for the other variables, the complexity of reconstruction depends on the assumptions of the model [39]. In general, one can't expect upscaled quantities like relative permeability and capillary pressure to have analytical expressions, thus one must rely on numerical computations of nonlinear functions [23].

There are specific cases where the procedure is severely simplified, for instance a sharp interface model where we expect the phase saturations to be piecewise constant with a discontinuity at the sharp interface. Hence, fine-scale saturation can be directly retrieved from a closed-form expression solely dependent on the depth of the CO2-brine interface h, without having to compute the inverse of a nonlinear capillary saturation function. For a fine cell with top depth T and bottom depth B, the reconstruction becomes

$$\hat{s}_n(h) = \begin{cases} 1, & t + h > B, \\ \frac{t+h-T}{B-T}, & T \le t + h \le B, \\ 0, & t + h < T. \end{cases}$$

The simplified sharp-interface model will be presented shortly.

4.2 Capillary pressure

The VE equivalent of capillary pressure is referred to as pseudo capillary pressure and equals the difference between the upscaled non-wetting phase pressure and upscaled wetting phase pressure.

The pseudo capillary pressure ensues directly from the hydrostatic pressure (15), and can be uniquely described by a reference depth z_0 and the depth h of the interface between CO2 and brine. Let $p_{c,i}$ be the capillary entry pressure at h. The pseudo capillary pressure for a column

of vertically segregated fluids is defined in terms of the reference height, here chosen to be the level of the caprock $z_0 = \zeta_T$, and is given by

$$P_c(h) = p_{c,i} + (\rho_w - \rho_n)gh(x,y)\cos(\theta),$$

where the dependence of the upscaled variable on the lateral coordinates is emphasized through $h = h(x,y)$.

The pseudo capillary pressure serves a similar role in the VE framework as the fine-scale pressure does in the full-dimensional framework in the sense that it provides a coarse-scale closure equation,

$$P_c(S_w) = P_n - P_w,$$

in which case the coarse saturation S_w is obtained by the inverse computation of the coarse capillary-saturation function, $P_c^{-1}(S_w)$.

4.3 Residual saturation

To implement residual saturation in the VE framework, an additional state variable is required, namely the maximum gas saturation obtained in each cell through simulation history, labeled $S_{n,\max}$. This variable is used to keep track of the maximum depth $h_{\max}$ of the layer of residual CO2 residing below the mobile CO2 plume and above the region of pure brine. Including residual saturation, $S_{n,\max}$ is related to $h_{\max}$ through

$$S_{n,\max} = \frac{h_{\max}}{H}(1 - s_{wr}),$$

where s_{wr} is the residual water saturation.

In the general case of a capillary fringe, S_n is not given by an analytical expression of h and $h_{\max}$ but requires computation of a nonlinear function $P_c^{-1}(S_w)$. Analytical relations are only provided in the simplified case of negligible capillary forces, as will be outlined in the next section.

4.4 Sharp interface model

In a CO2 storage setting, the vertical segregation is expected to happen quickly due to the large density contrasts between CO2 and brine, a difference of several hundred kilograms per cubic meter [39]. Following the work of [38], a measure of the importance of capillary forces, or more precisely the extent of any developed capillary fringe is given by

$$L_{cf} = \frac{\left(\frac{\partial p_c}{\partial s_n}\right)}{\Delta \rho g \cos(\theta)}.$$

Hence, a large density difference yields a thin capillary fringe. According to [39], vertical segregation by buoyant forces are expected to complete between 1 and 10 years, whereas capillary forces equilibrate (i.e. to develop a fully capillary fringe) after around 10 years. A typical injection operation lasts around 50 years. Hence, it is reasonable to assume that the fluid phases have reached hydrostatic equilibrium during the injection period, while the capillary fringe is still developing due to its slow diffusive nature dictated by the parabolic character of 3. During the injection period, one can thus neglect capillary forces and model the transition from brine to CO2 as a sharp interface. Moreover, due to the large density difference between CO2 and brine, the depth L_{cf} of the capillary fringe is usually several orders of magnitude smaller than the thickness of the formation and can be neglected even in the post-injection period with an acceptable loss in accuracy for long-term migration. Thus, the transition between CO2 and brine is often represented as an infinitely thin zone. This limiting case is referred to as a sharp interface assumption, characterized by a discontinuous transition from maximum brine saturation below the interface to maximum CO2 saturation above the interface.
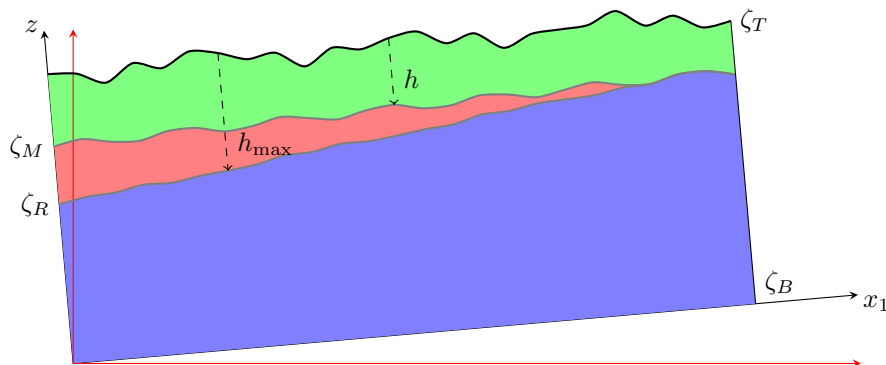

Figure 5: Sketch of a reservoir system used to derive the sharp interface VE model with residual saturation. The definitions ae similar to that of Figure 4 but now including a red zone of residual CO2 saturation of height $h_{\max}$. The sharp interface is located at ζ_M and the historically maximum depth reached is ζ_R.

Only a few years after injection stops, residual trapping contributes significantly to the trapping inventory [32]. Therefore, it is of interest to capture the effect of residual saturation. This involves hysteretic behavior as water reinvades pore space occupied by CO2. The residually saturated CO2 is vertically segregated from the historically deepest point reached (denoted ζ_R) and up to the bottom of the mobile plume (denoted ζ_M). Inclusion of residual saturation only amounts to modest changes in the sharp interface model. The VE representation of a particular fine-scale distribution is illustrated in Figure 5. The VE column is separated by three regions delineated by sharp interfaces; a bottom region extending from ζ_B to ζ_R consisting of pure brine, a middle region extending from ζ_R to ζ_M of brine and residual CO2, and a top region from ζ_M to ζ_T of CO2 and residual brine. The capillary pressure at the sharp interface located at ζ_M

equals the entry pressure required for CO2 to invade the brine filled region.

Fortunately, in a sharp interface model the fine-scale saturation is reconstructed by a simple analytical expression in terms of plume height $h = \zeta_P - \zeta_T$ and the historically maximum plume height $h_{\max} = \zeta_R - \zeta_T$ without having to rely on an inverse computation of a fine-scale capillary-saturation function, $s^{cap}(p_c)$. The variables h and $h_{\max}$ are related to the primary variables S_n and $S_{n,\max}$ through

$$
h = H\frac{S_n(1 - s_{wr}) - S_{n,\max}s_{nr}}{(1 - s_{wr})(1 - s_{nr} - s_{wr})},
$$
$$
h_{\max} = H\frac{S_{n,\max}}{1 - s_{wr}}. \tag{21}
$$

This allows us to swap primary variables from S_n and P_w to h and P_w, in which case we adopt an h-formulation of the governing equations that is particularly simple for sharp interface models. In the general case though, the difference between applying the h-formulation and the S-formulation is minor from a computational point of view [23], but the S-formulation retains most of the elements from conventional reservoir simulators and is therefore a more practical choice for implementing new physical effects [24].

The closed-form expression of reconstructed CO2 saturation in terms of h and $h_{\max}$ is given by

$$
\hat{s}_n = \begin{cases} 1 - s_{wr}, & z < \zeta_T + h, \\ s_{nr}, & \zeta_T + h \leq z \leq \zeta_T + h_{\max}, \\ 0, & z > \zeta_T + h_{\max}. \end{cases}
$$

For discrete cells, z spans a finite interval and the reconstructed saturation for a cell is given by an average of $1 - s_{wr}$ and s_{nr}, depending on how much of the cell constitutes mobile and residual CO2. Following the convention in Figure 8, let $\zeta_M = t + h$ and $\zeta_R = t + h_{\max}$ be the depth and maximum depth of the top plume, respectively. Using the following scaling factors for the mobile and residual part,

$$
a_M = \max\left[\min\left(\frac{\zeta_M - T}{H}, 1\right), 0\right]
$$
$$
a_R = 1 - a_M - \max\left[\min\left(\frac{B - \zeta_R}{H}, 1\right), 0\right]
$$

where T and B denotes the top and bottom of the fine cell, the reconstructed fine-scale saturation becomes

$$
\hat{s}_n = a_M(1 - s_{wr}) + a_R s_{nr}. \tag{22}
$$

Figure 6: VE representation of fine-scale saturation distribution including residual saturation.

The model equations become slightly more involved with the inclusion of residual saturation, but are still subject to simplification when considering a sharp interface where the rock parameters have negligible variation in the vertical direction [4]. From the fact that only one fluid phase is mobile on each side of the interface, the fine-scale mobilities in the respective regions are simplified,

$$\lambda_w(s_w) = \begin{cases} 0, & s_w = s_{wr} \\ \lambda_{w,e}, & s_w = 1 - s_{nr} \\ 1, & s_w = 1, \end{cases}$$

and similarly for CO2-mobility

$$\lambda_n(s_n) = \begin{cases} 0, & s_n < 1 - s_{wr} \\ \lambda_{n,e}, & s_n = 1 - s_{wr}, \end{cases}$$

where $\lambda_{w,e} = k_{rw,e}/\mu_w$ and $\lambda_{n,e} = k_{rn,e}/\mu_n$ and $k_{r\alpha,e}$ are endpoint relative permeabilites evaluated at their respective maximum saturations in a system where both phases are present. In general $k_{r\alpha,e} < 1$ due to additional resistance from the residual content of the other phase [17].

To facilitate a simple and appealing derivation of the sharp inteface model, we assume porosity is independent of depth and the permeability tensor has independent lateral and transversal components. The upscaled rock quantities then reduces to

$$\Phi = H\phi,$$

$$\boldsymbol{\kappa} = H\mathbf{K}_\parallel,$$

where $H = \zeta_B - \zeta_T$ is the depth of the aquifer. Upscaled phase saturations become

$$S_\alpha = (H\phi)^{-1}\phi \int_{\zeta_T}^{\zeta_B} s_\alpha \, dz = \frac{1}{H} \int_{\zeta_T}^{\zeta_B} s_\alpha \, dz,$$

with wetting and non-wetting components

$$S_w = \frac{1}{H}\Big[\int_{\zeta_T}^{\zeta_T+h} s_{wr} \, dz + \int_{\zeta_T+h}^{\zeta_T+h_{\max}} (1 - s_{nr}) \, dz + \int_{\zeta+h_{\max}}^{\zeta_B} 1 \, dz \Big],$$

$$= \frac{1}{H}\Big[s_{wr}h + (1 - s_{nr})(h_{\max} - h) + (H - h_{\max}) \Big].$$

$$S_n = \frac{1}{H}\Big[\int_{\zeta_T}^{h} (1 - s_{wr}) \, dz + \int_{\zeta_T+h}^{\zeta_T+h_{\max}} s_{nr} \, dz \Big],$$

$$= \frac{1}{H}\Big[(1 - s_{wr})h + s_{nr}(h_{\max} - h) \Big],$$

where $H = \zeta_B - \zeta_T$ is the depth of the aquifer.

Coarse-scale mobilities are simplified to

$$\mathbf{\Lambda}_\alpha = (H\mathbf{K}_\parallel)^{-1}\mathbf{K}_\parallel \int_{\zeta_T}^{\zeta_B} \frac{k_{r\alpha}(\hat{s}_\alpha)}{\mu_\alpha}\, dz = \frac{1}{H}\int_{\zeta_T}^{\zeta_B} \frac{k_{r\alpha}}{\mu_\alpha}\, dz.$$

Because the reconstructed fine-scale saturations $\hat{s}_\alpha$ are piecewise constant in each VE column, the integrals reduce to closed-form expressions,

$$
\begin{aligned}
\mathbf{\Lambda}_w &= \frac{1}{H\mu_w}\Big[\int_{\zeta_T}^{\zeta_T+h} k_{rw}(s_{wr})\, dz + \int_{\zeta_T+h}^{\zeta_T+h_{\max}} k_{rw}(1-s_{nr})\, dz + \int_{\zeta_T+h_{\max}}^{\zeta_B} k_{rw}(1)\, dz\Big] \\
&= \frac{1}{H\mu_w}\big[k_{rw,e}(h_{\max}-h) + (H-h)\big],
\end{aligned}
$$

$$
\begin{aligned}
\mathbf{\Lambda}_n &= \frac{1}{H\mu_n}\Big[\int_{\zeta_T}^{\zeta_T+h} k_{rn}(1-s_{wr})\, dz + \int_{\zeta_T+h}^{\zeta_T+h_{\max}} k_{rn}(s_{nr})\, dz + \int_{\zeta_T+h_{\max}}^{\zeta_B} k_{rn}(0)\, dz\Big] \\
&= \frac{h}{H\mu_n}k_{rn,e}.
\end{aligned}
$$

The remaining upscaled quantities in 18, R_α, $\hat{\mathbf{R}}_\alpha$, $\mathbf{N}_\alpha$ and Q_α depend on vertically variable phase densities and source terms and are thus not expressed analytically. For the brine phase they are given by

$$
\begin{aligned}
R_w &= H^{-1}S_w^{-1}\Big[\int_{\zeta_T}^{\zeta_T+h} \rho_w(z)s_{wr}\, dz + \int_{\zeta_T+h}^{\zeta_T+h_{\max}} \rho_w(z)(1-s_{nr})\, dz + \int_{\zeta_T+h_{\max}}^{\zeta_B} \rho_w(z)\, dz\Big] \\
\hat{\mathbf{R}}_w &= H^{-1}\mathbf{\Lambda}_w^{-1}\mu_w^{-1}\Big[\int_{\zeta_T+h}^{\zeta_T+h_{\max}} \rho_w k_{rw,e}\, dz + \int_{\zeta_T+h_{\max}}^{\zeta_B} \rho_w\, dz\Big] \\
\mathbf{N}_w &= H^{-1}\hat{\mathbf{R}}_w^{-1}\mathbf{\Lambda}_w^{-1}\mu_w^{-1}\Big[\int_{\zeta_T+h}^{\zeta_T+h_{\max}} \nu_p\rho_w k_{rw,e}\, dz + \int_{\zeta_T+h_{\max}}^{\zeta_B} \nu_p\rho_w\, dz\Big]
\end{aligned}
$$

Computing R_α, $\hat{\mathbf{R}}_\alpha$, $\mathbf{N}_\alpha$ requires solving the ODEs defining ρ_α and $\nu_{p,\alpha}$ for all values in the domain of integration, for each discrete cell and every time step. This quickly becomes computationally intractable. [5] proposes some alternatives to computing the integrals.

Pseudo capillary pressure is derived using the fact that the fine-scale capillary pressure should equal the entry pressure at the CO2-brine interface, h. If upscaled CO2 pressure is defined at the top of a VE column and upscaled water pressure at the bottom (the standard used in this thesis), pseudo capillary pressure in the sharp interface model is given by

$$P_c = P_n - P_w = p_e - \rho_n g h - \rho_w g(H - h).\qquad(23)$$

Because the depth h of the interface in the sharp interface assumption is directly related to the coarse saturations S_n and $S_{n,\max}$, the closure equations are trivial to compute. We now have a VE model of four equations satisfying the principle of mass conservation at the coarse scale that can be solved numerically.

In the fully-implicit VE scheme, one of the phase pressures is chosen as a primary variable, typically the water pressure P_w. As for the second primary variable there are two alternatives, either CO2 saturation, S_n, yielding the S-formulation, or the height of the CO2 column, h, yielding the h-formulation. An S-formulated VE model has the benefit of producing a system of algebraic equations that closely resembles conventional full-dimensional models [23], simplifying the implementation. However, computing the pseudo capillary pressure is more involved as it is expressed in terms of h, not S_n. In certain simplified models, e.g. a sharp interface model, the upscaled variables have simple analytical expressions, avoiding expensive computations of nonlinear algebraic systems. Therefore, the S-formulation is the preferred solution approach for the models considered in this thesis.

The relative permeability is often a nonlinear function of saturation. Thus, the flux across a face for a full-dimensional model is highly sensitive to deviations in the saturation. However, in a sharp interface VE model the fluids have either unit or zero relative permeability (assuming no residual saturations), implying that the flow is insensitive to any fine-scale nonlinearity [14]. However, a large variance in accuracy is expected near the sharp interface; if the interface deviates from its real height, cells near the interface will be assigned unit relative permeability when the true relative permeability is zero, and vice versa. This follows from the fact that all except one of the reconstructed fine cells will have unit or zero CO2 saturation. In other words, the VE model may predict flow of CO2 in regions only occupied by brine. The error is reduced by including a capillary fringe to model the transition between CO2 and brine, although this setting requires numerical computation of upscaled quantities [23].

The solution-reconstruction procedure in a fully-implicit VE model is summarized by the following pseudo-code.

Algorithm 1: Fully-implicit sharp interface model

Result: Solution vector $\{\boldsymbol{P_w}, \boldsymbol{S_n}\}$ of coarse multiphase flow equations

initialize fine state: $\{p_w^0,\ s_n^0\}$;

vertically integrate to get coarse state: $\{P_w^0,\ S_n^0\}$;

define upscaled rock properties;

  $\Phi = \int_{\zeta_T}^{\zeta_B} \phi\, dz$;

  $\boldsymbol{\kappa} = \int_{\zeta_T}^{\zeta_B} \mathbf{K}_\parallel\, dz$;

for $t = 0$ *to* T **do**

  reconstruct fine-scale water pressure;

    $\hat{p}_w = P_w^t + \rho_w g(z - \zeta_P)$;

  reconstruct fine-scale saturations;

    $h = h(S_n^{t+1}, S_{n,\max}^{t+1}), \quad h_{\max} = h_{\max}(S_{n,\max}^{t+1})$;

    $\hat{s}_n = a_M(h)(1 - s_{wr}) + a_R(h, h_{\max})s_{nr}$;

    $\hat{s}_w = 1 - \hat{s}_n$;

  compute the following upscaled variables analytically;

    $P_c^{t+1}(S_w^{t+1}) = p_e - \rho_n g h - \rho_w g(H - h)$;

    $P_n^{t+1} = P_w^{t+1} + P_c^{t+1}$;

    $\boldsymbol{\Lambda}_\alpha^{t+1} = \boldsymbol{\kappa}^{-1} \int_{\zeta_T}^{\zeta_B} \mathbf{K}_\parallel \lambda_\alpha(\hat{s}_\alpha)\, dz$;

  compute the following upscaled variables by numerical integration;

    $R_\alpha^{t+1}, \hat{\boldsymbol{R}}_\alpha^{t+1}, \boldsymbol{N}_\alpha^{t+1}, Q_\alpha^{t+1}$;

  compute coarse Darcy flux;

    $U_\alpha^{t+1} = -\boldsymbol{N}_\alpha^{t+1}\hat{\boldsymbol{R}}_\alpha^{t+1}\boldsymbol{\Lambda}_\alpha^{t+1}\boldsymbol{\kappa}\left(\nabla_\parallel P_\alpha^{t+1} - \rho_\alpha^{t+1}(g_\perp \cos(\theta)\nabla_\parallel \zeta_T + \boldsymbol{g}_\parallel)\right)$;

  solve coarse mass conservation equations for new state $\{P_w^{t+1}, S_n^{t+1}\}$;

end

reconstruct fine-scale solution $\{\hat{\boldsymbol{p}}_{\boldsymbol{w}},\ \hat{\boldsymbol{s}}_{\boldsymbol{n}}\}$ algebraically from VE assumption

---

5   Hybrid models

Vertical equilibrium models are limited to regions dominated by buoyant migration, and are only adequate substitutes for conventional 3D models for idealized scenarios of homogeneous high-permeable formations and vanishing viscous forces [39]. For injection scenarios in real reservoirs, these assumptions are violated by complex flow near injection wells and layered heterogeneities. Hybrid models are developed to provide a middle ground by combining the computational efficiency of VE models with the accuracy of fine-scale models. The idea is to utilize VE models in regions where the time of segregation 19 is sufficiently short, and 3D models in regions where viscous forces dominate and layers with sufficiently low permeability to make vertical segregation times long [21]. The resulting reservoir grid becomes multiscaled with regions modeled by different dimensionality. The governing coarse and fine equations of a hybrid model are similar to those of a pure VE and full-dimensional model, respectively, but evaluation of properties require special treatment in the transition between regions of different discretizations to ensure a consistent mapping between fine and coarse variables [36].

The literature contains several studies of hybrid models applied on different reservoir systems and with different physical effects included, i.e. [9], [21] and [11] to mention some. To our knowledge, there is a lack of acknowledged studies of fully-implicit sharp interface hybrid models with residual non-wetting saturation and capillary pressure included. Capillary exclusion has been shown to have a great impact on diffuse leakage and CO2 migration through low-permeability shales at the Sleipner field [13]. Accumulation of CO2 below low-permeable layers - and possible penetration - is not solely dependent on entry pressure, but also greatly influenced by residual trapping that favours less penetration by mitigating pressure build-up [19]. There exists a few studies that have developed hybrid models which include residual saturation and capillary pressure, i.e. [9], [21]. The latter was applied on multilayered systems and reported great agreement between the hybrid model and a full-dimensional model, but is based on the IMPES method that is generally less robust than a fully-implicit method for long-term CO2 migration with complex flow [39]. Hence, it is valuable to perform similar studies with a fully-implicit hybrid model to address the versatility of our extended hybrid framework.

A challenge with multilayered systems is homogeneous regions with semi-low permeability where the vertical flow of CO2 is too slow to assume instantaneous gravity segregation of CO2 and brine. Still, vertical dynamics is predominant and it is reasonable to simplify the modeling by neglecting horizontal fluxes. [21] developed a hybrid model that relaxes the VE assumption by solving the vertical dynamics as a one-dimensional problem rather than assuming instantaneous segregation. Herein, we retain the monolithic fully-implicit system and apply a different relaxation approach for columns where the VE assumption is potentially violated. The implementation of relaxed VE columns will be presented shortly.

5.1 Transition zones

A challenge of hybrid models is how to handle transitions between discretization regions numerically in a consistent way. In the governing equations, the flux is evaluated on faces delimiting neighboring cells. For interfaces between two fine cells or two VE cells of same type, the flux is evaluated as described in the governing equations for the full-dimensional and VE model, respectively. What is not as trivial is how the flux is evaluated at the transition between *different* discretization regions, where a discretization region is an assembly of adjacent cells with matching interfaces. Discretization regions for a full-dimensional, VE and hybrid model are shown in Figure 7.

(a) Full-dimensional   **(b)** VE   **(c)** Hybrid
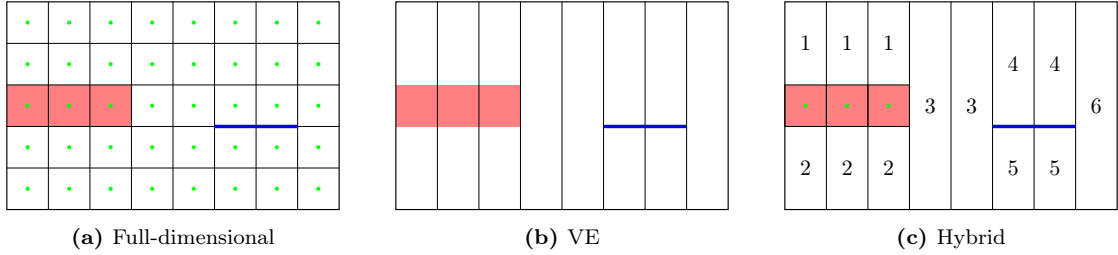
Figure 7: Discretization regions for a) full-dimensional, b) VE and c) hybrid model. Semi-permeable cells and faces are marked in red and blue, respectively. Black lines delineate cells, where fine cells are marked with green dots. Numbering represents VE cells of same discretization.

The interface between a fine cell and a coarse (VE) cell is characterized by a discontinuous top and/or bottom surface, so is the interface of VE cells of different heights. To obtain a consistent flux at the interface between neighboring cells, we introduce a set of virtual cells in the larger neighboring cell that match the vertical extent of the smaller neighboring cell, exemplified in Figure 8 for the transition between two VE columns of different heights.

Proper modeling of diffuse leakage through sealing layers is essential for reliable simulations of multilayered systems in the middle-to-long term, before all CO2 reaches the caprock. [36] performed a study of the hybrid model on the Utsira formation where diffuse leakage through three semi-permeable layers was represented by faces, i.e. as vertical VE-to-VE connections, with a fixed transmissibility multiplier of 10^{-4}. In other words, the impact of entry pressure and pressure gradients internally in the semi-permeable layers were represented indirectly by the transmissibility. Depending on the thickness and petrophysical properties of the layers, this may be an inaccurate approximation [1]. A better solution would be to have the flexibility to represent the semi-permeable layers as full-dimensional cells. This is substantiated by the fact that the thickness of the intraformational layers of shale in the Utsira formation varies from less than a meter to several meters [13], [44]. For the thickest layers, internal flow could turn out to be significant. Thus, the appropriate representation might as well be a combination of faces and cells.

In the original hybrid framework in MRST, fine cells are not only assigned to an imposed
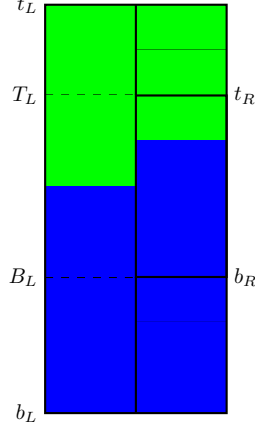
Figure 8: Illustration of a transition zone between two VE columns of different discretization, where dashed lines are introduced virtual cells. t and b are top and bottom of parent cell whereas T and B are top and bottom of any virtual cells. For VE columns with no virtual cells added, $t = T$ and $B = b$. Subscript L refers to the left column, and R to the right column. The right column is the smallest one and has no virtual cells added, i.e. $T_R = t_R$ and $B_R = b_r$.

fine region, but also to the columns above and below this region. If imposing a full-dimensional representation for the semi-permeable layers, all columns with the same lateral coordinate as the fine cells are turned full-dimensional as well. Hence, a face-representation of the semi-permeable layers is the only option facilitating a hybrid model. While a complete vertical extending full-dimensional region will accurately resolve internal flow in the semi-permeable layers, it defies our goal of modeling the spatially dominant intraformational high-permeable regions as VE. A modification of the hybrid grid preprocessor is therefore conducted to facilitate both a face representation and a full-dimensional representation. An illustration of the old and new formulation for two sealing layers is given in Figure 9.

With a full-dimensional representation of semi-permeable layers rather than a lower-dimensional face representation, horizontal fluxes are calculated through VE-to-fine horizontal transition regions in addition to the VE-to-VE horizontal transition regions that was applicable for face-representations. For vertical transitions, VE-to-VE is replaced by VE-to-fine, but since the interface is only across a single face we only need to introduce a single virtual fine cell for VE columns in the transition zone, regardless if modeling as VE-to-VE or VE-to-fine. Transition regions for the two different representations are shown in Figure 10. Additional computations arise from using cells to represent shales because flow behavior internally in the layer needs to be resolved. The benefit is that important physical effects such as capillary pressure, viscous forces and heterogeneous permeability are accounted for explicitly. By using faces to represent shales, entry pressure and the low permeability is implicitly captured by prescribing a low transmissibility. For thin shales where internal flow is of minor importance, this may be an adequate approximation [1], but for thicker shales the pressure gradient across the layer may be too complex to be approximated by a prescribed transmissibility. By resolving vertical dynamics using
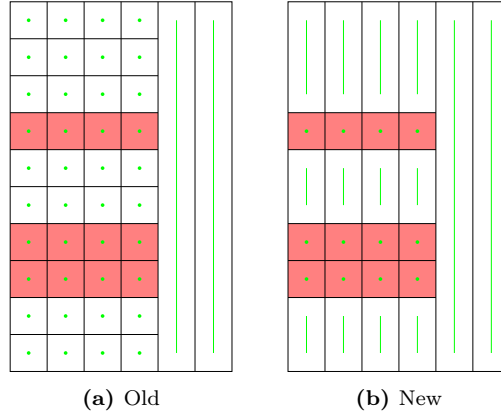
39

Figure 9: a) Old and b) New implementation of discretization regions in the vicinity of imposed fine cells (shaded in red). Cells modeled as full-dimensional marked by green dots, and cells modeled as VE marked by green lines.

full-dimensional cells, the transmissibility is correctly related to the permeability of the shale through its original formulation 7 without modification.
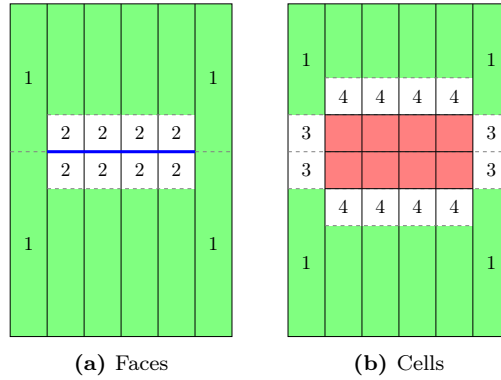

Figure 10: Transition regions for a semi-permeable layer a) faces and b) full-dimensional cells. Virtual cells are marked by dashed lines. Cells that are *modeled* as VE are shaded in green. Semi-permeable layers represented as faces are marked in blue, and as cells marked in red. Numbers represent the following transition zones:
1: VE-to-VE Horizontal.
2: VE-to-VE Vertical.
3: VE-to-Fine Horizontal.
4: VE-to-Fine Vertical.

NOT SURE IF INCLUDING THIS. Modeling diffuse leakage is sort of already represented in Figure 10. For the purpose of modeling diffuse leakage, it is apposite to exemplify how calculation of fluxes are altered at a transition zone by considering two low-permeable layers of different size bounded by high-permeable regions. The appropriate transition zones are illustrated in Figure

11, where cells and faces are used represent the thick layer and thin layer of shale, respectively. For the flux across the interfaces to be consistent we must introduce virtual fine cells in the VE columns and reconstruct fine-scale variables in the calculation point of the virtual cells, which are by default located at the center for fine cells. To model diffuse leakage, the thick shale layer incorporates capillary pressure and internal flow, whereas the thin shale layer represents capillary pressure slightly less accurate by a modified transmissibility. We refer to [36] for a thorough description of different discretization regions.
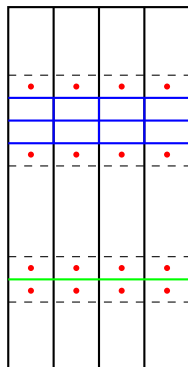

Figure 11: Diffuse leakage modeled either as vertical VE-to-VE transition using lower-dimensional faces (marked in green) or as vertical VE-to-fine transition using full-dimensional cells (marked in blue). Virtual cells are introduced (dashed lines) in the bounding VE columns, where red dots show the calculation points of reconstructed variables.

5.2   Capillary pressure

The pseudo capillary pressure (23) is unchanged by including residual saturation, because the fine-scale capillary pressure still equals the entry pressure at the CO2-brine interface and the hydrostatic pressure distribution of a phase is unaffected by the residual content of another immobile phase. Reconstruction of capillary pressure at the center of virtual fine cells, as required for calculation of fluxes, simply uses the capillary function on the reconstructed saturation in the virtual cells, $\hat{p}_c = p_c(\hat{s}_w)$. For a sharp interface model there is no need for numerical integration since the expression is analytically given by $\hat{p}_c = p_e$. The pseudo capillary pressure in a virtual VE cell is calculated from 23 with h and H corresponding to the local height of the mobile plume and height of the virtual cell, respectively. Reconstruction of primary variables will be outlined later in this chapter.

5.3 Residual saturation

Implementation of residual saturation in a hybrid model is essentially the same as for fine models and conventional VE models, but with particular care in transitions between regions of different discretizations. The main factors that invalidate the conventional implementation of residual saturation is the long time scale for diffuse leakage and late migration at the boundaries of semi-permeable layers. The former is likely to yield advancing plume tips due to slow gravity drainage even during late stages of the simulation [21]. Because the tail of the plume moves faster than the tip [26], the migrating plume may be immobilized before it reaches the top of the column. The vertical distribution of mobile and residual saturation given in Figure 4 is no longer applicable, as there may be additional residual parts isolated from the top plume that has penetrated through semi-permeable layers at later stages in the simulation.

A full-dimensional model is more appropriate in the vicinity of semi-permeable layers characterized by slow gravity drainage [21], but with multiple semi-permeable layers the number of full-dimensional cells quickly grows too large for a hybrid model to yield any significant advantages over a full-dimensional model. Alternatively, we retain a reduced dimensionality but relax the VE assumption. The idea is to preserve the reduced dimension. Whereas [21] resolved slow vertical drainage as independent one-dimensional problems, we herein base it on a treatment of coarse fluxes from the relevant transition zones that allow us to discern the top segregated plume from late-stage isolated plumes originating from semi-permeable layers.

5.3.1 Immobilization of plume

The VE assumption implies that residual CO_2 is distributed from the bottom of the mobile part of the plume with height h and down to a depth $h_{\max}$ as derived from the maximum coarse saturation $S_{n,\max}$. However, for multilayered systems it is customary for CO_2 to have a significant horizontal spread at intermediate depths as well, not only below the caprock. That is, CO_2 originates from multiple semi-permeable layers, in which case residual CO_2 is distributed vertically from the *bottom* of the layers, not only from the plume residing at the top of the formation. Moreover, insignificant diffuse leakage from semi-permeable layers combined with retardation of the leading edge of the plume may immobilize the plume before reaching the caprock [26].

The conventional VE model described in 4.3 does not account for additional late-stage migrating plumes separated from the buoyant segregated plume at the top of the formation. In turn, this may lead to an overestimate of the mobile plume and consequently an inaccurate estimate of fluxes to neighboring columns. Fortunately, it is possible to account for these additional plumes, potentially immobilized, in the VE framework by a naive consideration of fluxes. The idea is to locate VE columns transitioning to a lower layer (that be VE-to-fine transitions or VE-to-VE transitions), and keep track of the accumulated upward fluxes across the transitions. Since flow of CO_2 is primarily buoyancy driven after penetrating a semi-permeable layer, these

fluxes will provide an estimate of how much CO2 in the column originates from the bottom.

The endpoints of low-permeable layers and lenses are also regions where the VE assumption may be violated. In contrast to VE columns transitioning to lower layers, the relevant transition is between VE columns of different discretizations. That is, we need to keep track of fluxes across *horizontal* VE-to-VE transition zones, as these are responsible for late buoyant migration at the endpoints and allow us to reproduce the residual content nearby. Combined with the coarse saturations S_n and $S_{n,\max}$ we have enough information to reproduce the vertical saturation distribution in relaxed VE columns.
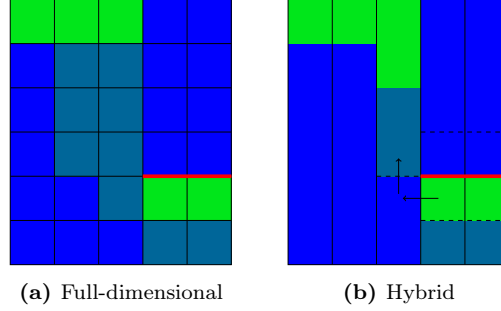

(a) Full-dimensional	**(b)** Hybrid

Figure 12: Distribution of CO2 resulting from horizontal flux at the endpoint of a semi-permeable layer (marked in red) for a) full-dimensional and b) hybrid model. The weak green color represents residual CO2 saturation while strong green represents mobile CO2. Dashed lines in hybrid grid delineate virtual cells. Note that the column next to the semi-permeable layer has been assigned a larger amount of CO2 than the same column in the full-dimensional model, as a result of the net horizontal flux being converted to an equivalently large vertical flux in the first neighboring VE cell (illustrated by black arrows)

Though, there will be an inevitable loss in accuracy compared to the fine-scale solution due to unaccounted horizontal fluxes beyond the endpoints. The VE assumption will by definition assume exclusive buoyant migration in virtual VE columns and therefore underestimate the width of the migrating plume in veHorizontal regions, as illustrated in Figure 12. This is an inevitable artifact of the VE model. The residual part is reconstructed assuming the net horizontal flux from the neighboring VE column to a virtual VE column is converted to an equivalently large vertical flux upward from the top of the virtual VE column. Therefore, the saturation reconstruction for virtual VE columns is essentially similar to that of VE columns with an upward flux at the bottom. Reconstructed saturation in a multilayered system for the old and new implementation of residual saturation is shown in Figure 13, exemplifying a case with multiple immobilized plumes in the same column, originating either from the bottom or the endpoints of semi-permeable layers.

5.3.2 Implementation

To incorporate residual saturation in the hybrid model that facilitates late-stage migration, but without the extra computational burden of representing VE cells as fine cells, we intro-
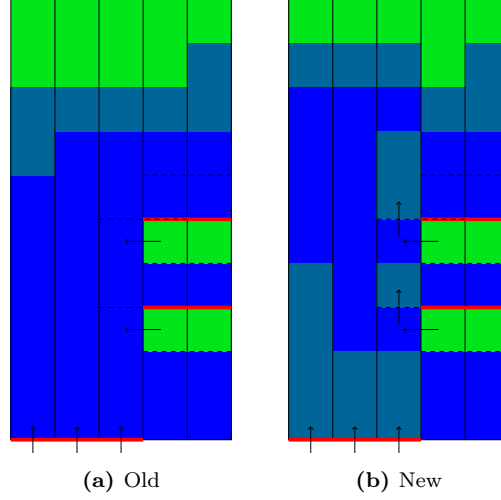
(a) Old   **(b)** New

Figure 13: Distribution of CO2 resulting from bottom and horizontal fluxes from semi-permeable layers (marked in red) for a) old implementation and b) new implementation of residual saturation for a multilayered system. The hybrid model introduces relaxed VE columns to trace plumes originating from semi-permeable layers. The weak green color represents residual CO2 saturation while strong green represents mobile CO2. Dashed lines in hybrid grid delineate virtual cells, and black arrows denote fluxes from semi-permeable layers.

duce two new state variables, $u_\Sigma^b = \sum_{i=1}^n u_i^b \Delta t_i$ and $u_{\Sigma,\max}^b = \sum_{i=1}^k u_i^b \Delta t_i$. The former is the accumulated sum of fluxes at current time step n up from the bottom of a VE column transitioning to a lower low-permeable layer. The latter describes the same but accumulation is only up to time step $k \leq n$ where the current $S_{n,\max}$ was reached. Similarly, the horizontal fluxes $u_\Sigma^h = \sum_{i=1}^t u_i^h \Delta t_i$ and $u_{\Sigma,\max}^h = \sum_{i=1}^k u_i^h \Delta t_i$ across VE columns of different discretizations are stored. The variables $u_{\Sigma,\max}^x$ is necessary to ensure a consistent maximum saturation $S_{\max}^T$ of the plume residing below caprock, distinguished from late migrating plumes emanating from semi-permeable layers.

The original expressions 21 for h and $h_{\max}$ are retained for all cells except columns with a relaxed VE assumption. There are three types of VE cells that obtain a modified expression.

- VE cells transitioning to a layer below in a VE-to-VE or VE-to-fine transition region, queried by $B = b$ and $T \neq t$, where B and T are the bottom and top depths of the virtual fine cell as part of the VE cell above the interface, using the convention in Figure 8

- VE cells transitioning to neighboring VE cells of different discretization, represented as a VE-to-VE horizontal transition zone. To yield a rising plume in the associated virtual VE cells, we only select the virtual cells that do not share top surface with the parent VE cell. For the two virtual cells shown in Figure 12, only the lower one satisfies this criteria.

- VE cells that satisfy the two above requirements, associative of rising plumes both as diffuse leakage and from endpoints of semi-permeable layers, as illustrated in Figure 13.

44

There are three regions to distinguish; mobile CO2, S_{mob}, buoyantly segregated at the top with maximum saturation reached $S_{\max}^T$, and net late-stage CO2 migrating from semi-permeable layers, S_B. The latter is calculated from the accumulated fluxes from adjacent semi-permeable layers. For a VE cell j, the calculation is

$$S_u(j) = \frac{u_\Sigma^b + \sum_{i \in \mathcal{D}_h(j)} u_{\Sigma,i}^h}{\Phi V} = S_{u,b} + \sum_{i \in \mathcal{D}_h(j)} S_{u,hi},$$

where $u_{\Sigma,i}^h$ is the accumulated flux from the i'th horizontal neighboring semi-permeable layer out of $\mathcal{D}_h$ in total, with $S_{u,hi}$ the corresponding saturation, and $S_{u,b}$ the saturation resulting from diffuse leakage from a semi-permeable layer at the bottom. Similarly we have that the accumulated bottom flux up to the time step where current $S_{\max}$ was first reached yields a saturation

$$S_{B,\max}(j) = \frac{u_{\Sigma,\max}^b + \sum_{i \in \mathcal{D}_h(j)} u_{\Sigma,\max,i}^h}{\Phi V},$$

The maximum saturation from the top plume is given by $S_{\max}^T = S_{\max} - S_{B,\max}$, from which the maximum reached depth of the top plume evaluates to

$$h_T = \max\left(H \frac{S_{\max}^T}{1 - s_{wr}},\ 0\right).$$

The top depth of the plume rising from a semi-permeable layer i is given by the expression

$$d_{ki} = \max\left[\min\left(\bar{H}_i(1 - \bar{S}_{F,ki}),\ \bar{H}\right),\ h_T\right],$$

where for a semi-permeable layer at the bottom of the column we have $ki = b$ and

$$\bar{H}_i = H,$$
$$\bar{S}_{F,b} = S_{u,b}/s_{nr},$$

where H is the height of the VE column. For semi-permeable layers at VE-to-VE horizontal transition regions we have $k = h$ and

$$\bar{H}_i = H_i,$$
$$\bar{S}_{F,hi} = S_{u,hi}/\left(\frac{H_i}{H} s_{nr}\right),$$

where $H_i = T_i - t$ is the height from the top of the parent VE cell, t, to the top of the virtual VE cell i, T_i. The expression for normalized plume saturation $\bar{S}_{F,hi}$ follows from the fact that the maximum amount of immobilized CO2 in the parent cell originating from semi-permeable layer i is $\frac{H_i}{H} s_{nr}$, so that $\bar{S}_{F,hi} \in [0, 1]$.

The top depth of all individual plumes stacked on top of each other from the bottom, labeled

h_B, is given by

$$h_B = \max(H - \Delta h_B, \, h_T),$$

$$\Delta h_B = (H - d_b) + \sum_{i \in \mathcal{D}_h(j)} (H_i - d_{hi}),$$

where $\Delta h_B = h_T$ implies that the VE column is entirely filled with residual saturation and the column satisfies VE. Hence, in the hybrid model, non-segregated plumes are assigned residual saturation, but once they reach the top VE is justified and additional fluxes of CO2 will immediately rise and accumulate as a mobile layer beneath the top.

With these variables, we can define the net height reached by all plumes in a relaxed VE cell to be

$$h_{\max} = h_T + (H - h_B). \tag{24}$$

Finally, total residual content in the column is

$$S_{nr,tot} = s_{nr} \frac{h_{\max}}{H},$$

which yields the mobile saturation

$$S_{mob} = S - S_{nr,tot},$$

and the height of the mobile plume on the top

$$h = H \Big(\frac{S_{mob}}{1 - s_{wr} - s_{nr}} \Big). \tag{25}$$

With these modified expressions for h and $h_{\max}$, the coarse mobilities and associated phase fluxes are also modified for relaxed VE columns.

5.4   Coupled equations

The governing equations in a hybrid framework couple the fine-scale and coarse-scale formulations. From the fact that the upscaled equations in a VE model have principally the same form as the fine-scale equations, we are in a position to formulate a general set of algebraic equations for a hybrid model. For this we need two indicator functions. The first one, $C(i)$, returns the column-index of cell i in the hybrid grid, where all cells vertically stacked on top of each other share the same column-index. Secondly, the indicator $V(i)$ returns the discretization region of cell i. As an example, two cells j and k that are vertically stacked but delimited by a sealing face share the same column-index, i.e. $C(j) = C(k)$, but are from different VE regions, i.e. $V(j) \neq V(k)$. All fine cells c_f are assigned the same discretization, by default $V(c_f) = 1$. Moreover, let $N(i)$ denote the set of neighboring cells connected to cell i. With this in hand, the

governing hybrid equations are compactly written as

$$\frac{\Gamma_{i,\alpha}^{n+1} - \Gamma_{i,\alpha}^{n}}{\Delta t_n} - \sum_{j \in N(i)} f_{ij}(\Pi_\alpha^{n+1}) = \Psi_i^{n+1}, \tag{26}$$

The definition of the accumulation and source terms now depend on the particular cell i by

$$\Gamma_{i,\alpha} = \begin{cases} \phi_i s_{i,\alpha} \rho_\alpha, & V(i) = 1, \\ \Phi_i S_{i,\alpha} R_\alpha, & V(i) \neq 1. \end{cases}$$

$$\Psi_i = \begin{cases} q_i, & V(i) = 1, \\ Q_i, & V(i) \neq 1. \end{cases}$$

The flux term f_{ij}, the variable set $\Pi_{ij,\alpha}$ used to compute the flux now depends on the column-indices and discretization regions of cell i and j, either given as fine-scale variables, coarse-scale variables or a combination thereof,

$$\Pi_{ij,\alpha} = \begin{cases} (p_\alpha, \rho_\alpha, \lambda_\alpha(s_\alpha), z), & fineInternal \\ (P_\alpha, R_\alpha, \Lambda_\alpha(\hat{s}_\alpha), Z), & veInternal \\ (\hat{p}_\alpha^{ij}, \hat{\rho}_\alpha^{ij}, \lambda_\alpha(\hat{s}_\alpha^{ij}), z), & veToFine\&veVertical \\ (\hat{P}_\alpha^{ij}, \hat{R}_\alpha^{ij}, \Lambda_\alpha(\hat{s}_\alpha^{ij}), Z), & veHorizontal \end{cases}$$

A hat denotes a reconstructed variable, and a superscript ij refers to variables that have been reconstructed for the virtual cell, i or j, in the discontinuous transition ij. Note that the coarse mobility Λ_α depends on the reconstructed saturation $\hat{s}_\alpha$ through integration of the fine-scale relative permeability $k_{r\alpha}$, although analytically expressed in a sharp-interface setting. The reconstructed phase density is evaluated from the reconstructed pressure, i.e. $\hat{\rho}_\alpha^{ij} = \rho_\alpha(\hat{p}_\alpha^{ij})$. The coarse depth Z represents the top and bottom of the formation for gas phase and liquid phase, respectively. Reconstructed gas saturation in the virtual cell is based on an average value over the cell (see Section 4.1, while reconstructed liquid pressure is evaluated at the center of virtual fine cells and at the bottom of virtual VE cells, as illustrated in Figure 14.

5.5   Selection of discretization regions

Manually dividing the computational grid into discretization regions is a cumbersome process, especially for real reservoirs of complex geometry. Therefore, we propose an automatic selection of discretization regions according to geometry and petrophysical properties. The partitioning of different VE regions is based on a cell connectivity matrix representing the transmissibility
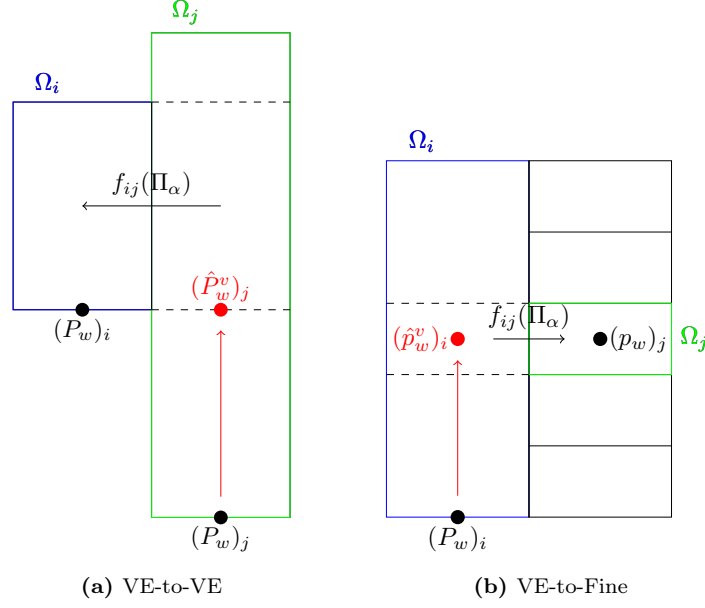
47

Figure 14: Reconstruction of water pressure (denoted with hat) in a) VE-to-VE horizontal transition zone and b) VE-to-Fine horizontal transition zone. $f_{ij}(\Pi_\alpha)$ represents the flux function between cell i and j. Note the distinguish between coarse variables P_w and fine-scale variables p_w.

between adjacent VE cells,

$$
(C_c)_{ij} = \begin{cases} 1, & M(i, D(j)) = 1, \\ 0, & \text{else,} \end{cases}
$$

where $D(j)$ is the discretization region of cell j and $M(i, J)$ is the number of cells with discretization region $J = D(j)$ that cell i is connected to with transmissibility above some prescribed threshold. Thus, if VE cell i is an internal VE column its neighboring VE cells have the same discretization region J, implying that $M(i, J) > 1$ and $(C_c)_{ij} = 0$. Cell i then belongs to the same discretization regions as its neighbors so the columns are merged. In contrast, if i has at least one discontinuous connection to a neighboring VE column, then $M(i, J) = 1$ and $(C_c)_{ij} = 1$, in which case the columns are separated into different discretization regions.

The faces representing a transition from imposed fine cells to VE columns are treated separately in order to collect all fine cells into a single discretization region $V = 1$. Hence, imposed fine regions is a required input from the user. Alternatively, the selection can be made adaptive by querying all cells satisfying a certain criteria, for instance having permeability below a prescribed threshold. The selection algorithm is described in more details in [36].

5.6 Reconstruction

Similar to vertical equilibrium models, VE columns in a hybrid model need to have fine-scale variables reconstructed, both for computation of upscaled variables and for comparison to full-dimensional models. The same principles for reconstruction apply, but the expressions are modified for VE columns by accounting for the hysteretic variable $S_{n,\max}$. Moreover, for relaxed VE columns we also need to account for accumulated fluxes from each semi-permeable layer to locate isolated late migrating plumes.

5.6.1 Fine-scale saturation

Even with a non-zero residual saturation, the reconstructed fine-scale CO_2 saturation still has an analytical expression in the sharp interface setting but now includes a dependency on the residual parts left in the wake of migrating plumes, which for relaxed VE columns are described in terms of the depths d_b and d_{hi}.

Reconstruction of fine-scale CO_2 saturation given by 22 requires modifications for relaxed VE columns to account for immobilized plumes, particularly the expression for the residual content, now given by

$$a_R = \min(a_{RT} + a_{RS},\, 1 - a_M),$$

where a_{RT} represent the residual part coming from the top plume (i.e. a_R in the original formulation 22) and a_{RS} the residual part from migrating plumes from sealing layers. Let T and B be the top and bottom depths of fine cell c of a column, $H_{tk} = t + H_k$ the top depth of the virtual cell bounded by sealing layer k and $h_{tk} = t + h_k$ the top depth of the plume rising from sealing layer k. There are four scenarios in which this plume may contribute to the residual content of fine cell c,

- c is located partly below the bottom of the plume and not above top of the plume, given by the indicator $I_b = h_{tk} \leq T < H_{tk} \quad \& \quad B > H_{tk}$

- c is located partly above the top of the plume and not below the bottom of the plume. Indicator: $I_t = h_{tk} < B \leq H_{tk} \quad \& \quad T < h_{tk}$

- c covers the entire plume. Indicator: $I_o = T < h_{tk} \quad \& \quad B > H_{tk}$

- entire c is inside the plume. Indicator: $I_i = h_{tk} \leq T < H_{tk} \quad \& \quad h_{tk} < B \leq H_{tk}$

With the help of these indicators, we have

$$a_{RS} = \frac{1}{(B-T)} \sum_{k \in \mathcal{D}_h} \big[(H_{tk} - T)I_b + (B - h_{tk})I_t + (H_{tk} - h_{tk})I_o + (B - T)I_i\big].$$

The expression for the mobile ratio a_M is unchanged for relaxed VE columns.

5.6.2 Fine-scale phase pressures

In section 4.1 we argued why the Dupuit approximation is the appropriate way to reconstruct fine-scale pressure in VE columns. The approximation still holds for VE columns in a hybrid model, but not necessarily for evaluation of fluxes in relaxed VE columns. Thus, reconstructing phase pressures from a strict hydrostatic assumption is not appropriate in these regions [20]. The reconstruction needs to account for a nonuniform distribution of CO2 and brine, but still reproduce a hydrostatic profile in the limits where VE is applicable. In this regard, [20] proposes a more general saturation-weighted reconstruction,

$$\hat{p}_w = P_w - \int_b^{z_r} \left((\hat{s}_n \rho_n + \hat{s}_w \rho_w) g + \hat{s}_n \frac{\partial p_c}{\partial z} \right) dz, \tag{27}$$

where z_r is the point of interest where pressure should be reconstructed and $\bar{s}_\alpha$ are saturations normalized by the residual content.

It is worth mentioning that the reconstruction 27 is only used to evaluate fluxes between different discretizations and does not enter as a primary variable. 27 is specific for models with a capillary fringe considering that the presence of *two* mobile phases inside the fringe necessitates a saturation-weighted hydrostatic profile within this zone. In the sharp interface model outlined in 4.4 weighting by saturation becomes redundant because phases at residual saturation do not induce any pressure, and there will only be a single mobile phase present in each of the three distinct vertical regions shown in Figure 4. With these simplifications, 27 becomes

$$\begin{aligned} \hat{p}_w &= P_w - \int_{z_r}^d \rho_n g \, dz - \int_d^b \rho_w g \, dz \\ &= P_w - \rho_n g(d - z_r) - \rho_w g(b - d), \end{aligned} \tag{28}$$

where $d = \max(t + h, z_r)$ is the maximum of the depth of the mobile plume $t + h$ and the point of interest z_r. It should be emphasized that z_r is chosen to be the center and bottom of virtual fine cells and virtual VE cells, respectively. The reconstructed pressure in virtual cells is independent of the historically maximum depth of the CO2 plume and therefore has the same formulation regardless of residual content. In virtual fine cells, CO2 pressure is evaluated as $\hat{p}_n = \hat{p}_w + p_c(\hat{s}_w)$, that is the capillary pressure function is evaluated on the reconstructed saturation in the virtual cell. The coarse gas pressure in virtual VE cells is given by $\hat{P}_n = \hat{P}_w + P_c(\hat{h})$, where $\hat{P}_w$ is the coarse water pressure reconstructed at the bottom of the virtual VE cell, and P_c is the pseudo capillary pressure in the virtual VE cell that depends on the local height $\hat{h} = t + h - T$ of the plume in this cell.

5.7 Solution strategy

Once the primary variables are defined for each cell, that being VE, fine-scale or virtual, and the appropriate expressions for the interface fluxes have been established, the system equations are ready to be solved. By using the S-formulation the full problem can be solved monolithically as a set of nonlinear algebraic equations.

A pseudo-code for the hybrid solution scheme is provided below. The equation system and numerical methods are similar to that for the VE and full-dimensional models, but now with specific treatment of transition regions.

Algorithm 2: Hybrid sharp interface model

Result: Solution vectors $\{\boldsymbol{p_w}, \boldsymbol{s_n}\}$ and $\{\boldsymbol{P_w}, \boldsymbol{S_n}\}$ for hybrid multiphase flow equations

initialize states for fine and coarse parts of domain: $\{p_w^0,\ s_n^0\}$;

vertically integrate in VE regions to get coarse state: $\{P_w^0,\ S_n^0\}$;

define state-independent upscaled properties;

$\qquad \Phi = \int_{\zeta_T}^{\zeta_B} \phi\, dz$;

$\qquad \boldsymbol{\kappa} = \int_{\zeta_T}^{\zeta_B} \mathbf{K}_\parallel\, dz$;

for $t = 0$ *to* T **do**

    VE cells: calculate $h = h(S_n^{t+1}, S_{n,\max}^{t+1})$ and $h_{\max} = h_{\max}(S_{n,\max}^{t+1})$;

    relaxed VE cells: calculate $h = h(S_{mob}^{t+1})$ and $h_{\max} = h_{\max}(h_B^{t+1}, h_T^{t+1})$;

    compute mobile content $a_M = a_M(h)$ and residual content $a_R = a_R(h, h_{\max})$ in
      virtual cells;

    if *Horizontal VE-to-VE* **then**

        reconstruct coarse phase saturations in virtual VE cells;

            $\hat{S}_n = a_M(1 - s_{wr}) + a_R s_{nr}$;

            $\hat{S}_w = 1 - \hat{S}_n$;

        calculate water height Δz and CO2 plume height Δh below *bottom B* of virtual
         VE cell;

            $\Delta h = \max(t + h - B,\ 0)$;

            $\Delta z = b - B - \Delta h$;

        reconstruct water pressure at bottom of virtual VE cells;

            $\hat{P}_w = P_w^b - \rho_w g \Delta z - \rho_n g \Delta h$;

    end

    if *VE-to-Fine or Vertical VE-to-VE* **then**

        reconstruct phase saturations in virtual fine cells;

            $\hat{s}_n = a_M(1 - s_{wr}) + a_R s_{nr}$;

            $\hat{s}_w = 1 - \hat{s}_n$;

        calculate water height Δz and CO2 plume height Δh below *center C* of virtual
         fine cell;

            $\Delta h = \max(t + h - C,\ 0)$;

            $\Delta z = b - C - \Delta h$;

        reconstruct water pressure at bottom of virtual fine cells;

            $\hat{p}_w = P_w^b - \rho_w g \Delta z - \rho_n g \Delta h$;

    end

    compute upscaled variables: $P_c^{t+1}, \boldsymbol{\Lambda}_\alpha^{t+1}, R_\alpha^{t+1}, \hat{\boldsymbol{R}}_\alpha^{t+1}, \boldsymbol{N}_\alpha^{t+1}, Q_\alpha^{t+1}$;

    compute fine and coarse Darcy fluxes: $\boldsymbol{u}_\alpha^{t+1}$ and $\boldsymbol{U}_\alpha^{t+1}$;

    solve equations 3 and 18 for new states $\{p_w^{t+1},\ s_n^{t+1}\}$ and $\{P_w^{t+1},\ S_n^{t+1}\}$;

end

VE cells: reconstruct $\{\hat{\boldsymbol{p}}_w,\ \hat{\boldsymbol{s}}_n\}$ algebraically from VE assumption, 20 and 22;

5.8 Trapping distribution

A comprehensive trap analysis is not possible in the original implementation the hybrid model in MRST, because neither residual saturation is included nor localization of By extending the original implementation of hybrid models in MRST with residual saturation and localization of intermediate, semi-permeable structural traps, it is now possible to conduct a comprehensive trap analysis, disregarding dissolution and mineral trapping, an invaluable tool to establish an optimization framework applicable for hybrid models.

While the elements of the trapping inventory for pure VE models remain unchanged for a hybrid model, the separate trap analyses conducted for each subdomain must be assembled to yield a trapping inventory applicable for the entire formation. Moreover, calculation of masses from different categories are modified for relaxed VE columns. In the following we briefly go through the categorization of masses for a hybrid model.

SHOW IMPLEMENTATION ... not done yet ...

6 Numerical simulations

In this section we outline the setup for numerical simulations of a set of CO2 injection scenarios. To demonstrate the wide applicability of hybrid models, we first consider simplified synthetic 2D formations with gradually added complexity, a synthetic multilayered 3D formation and conclude with an application to real data from the Utsira formation. The synthetic scenarios will primarily serve as a test suite for presenting the extended hybrid framework and for a quantitative comparison with VE and full-dimensional models.

6.1 Synthetic two-dimensional formations

As our first test case, we consider a highly simplified formation consisting of a single low-permeable layer embedded in a high-permeable rock. To merely present the hybrid framework the formation is set strictly horizontal. There is a tiny hole in the low-permeable layer to mimic a complete fracture where CO2 leaks immediately. Accumulation below the low-permeable layer and diffuse leakage invalidates the VE assumption, and a conventional VE model loses information about the non-uniform permeability and how it affects plume migration. Apart from the low-permeable layer, the VE assumption holds for the remaining high-permeable region. Hence, the problem setting is well suited for a hybrid model. We wish to clarify the inappropriateness of using VE columns in the entire domain by comparing the hybrid model with a pure VE model in addition to a full-dimensional model. The hybrid partitioning is shown in Figure 15. Notice that full-dimensional cells are imposed near the well and at the open left boundary. The latter is imposed to ensure the boundary conditions are fulfilled.
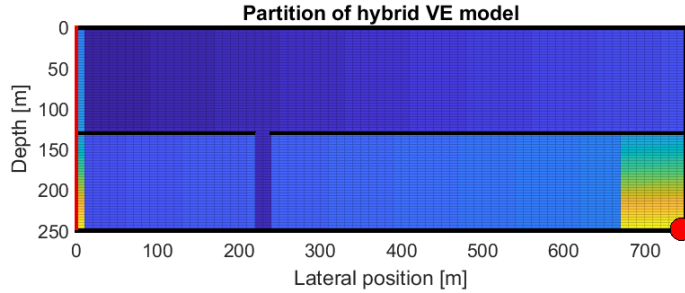

Figure 15: Partitioning of the synthetic two-dimensional horizontal domain into different discretization regions.

Next we generate a multilayered synthetic reservoir to add complexity and mimic a real storage setting. To this end, we set up a heterogeneous formation with multiple low-permeable layers of different permeability and thicknesses. The layers are responsible for diffuse leakage and subsequent late migrating plumes. Combined with a highly nonlinear relative permeability

54

function that slows down migration significantly during the drainage-imbibition process [10], the VE assumption is likely to be violated in multiple parts of the domain.

The appropriateness of using a hybrid model with relaxed VE columns will be demonstrated, with particular focus on the novel implementation of residual saturation and volume mismatch with the full-dimensional model.

The hybrid partitioning of the domain is provided in Figure 16. In this test case we use an adaptive grid generation that represents low-permeable layers/lenses either as full-dimensional cells or two-dimensional faces, depending on the thickness.
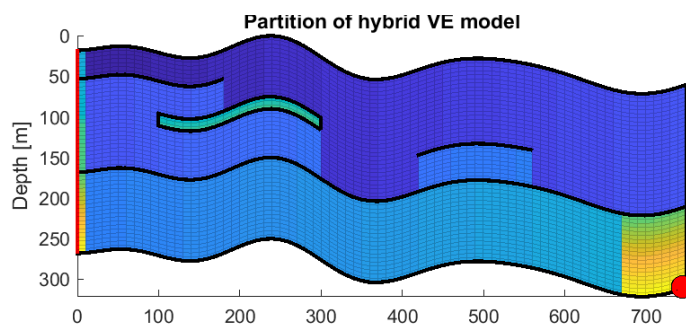
Figure 16: Partitioning of the synthetic two-dimensional sloped domain into different discretization regions.

6.2 Synthetic three-dimensional formation

THIS SETUP WILL BE MODIFIED: A TALLER FORMATION WITH MULTIPLE SEMI-PERMEABLE LAYERS STACKED VERTICALLY AND PERMEABLE CAPROCK. GOAL: DEMONSTRATE CAPILLARY EXCLUSION AND CALCULATE TRAPPING INVENTORY (TO BE COMPARED WITH FULL-DIM MODEL.

Simulation of reservoir dynamics in three dimensions is where a full-dimensional model suffers and the benefits of a hybrid model really materializes. To demonstrate, we generate a synthetic, sloped three-dimensional grid with multiple semi-permeable layers modeled as full-dimensional cells, as illustrated in Figure 17. Curvatures of the formation are exaggerated to make the proportion of formation volume subject to structural traps significant, facilitating a trap analysis of diverse mass distributions.

6.3 Idealized injection scenario at the Sleipner field

Now that the applicability of the hybrid model has been verified for synthetic cases of various complexity, we perform a comparison of the models on geological data from a real multilayered formation that would, in theory, benefit from a hybrid model. Herein, we select this section of
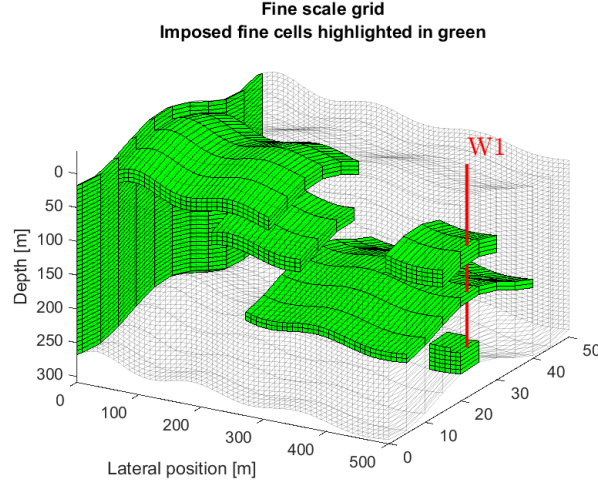
Figure 17: Highlight of semipermeable layers and imposed fine regions for the hybrid grid of a synthetic sloped 3D domain.

the Sleipner field, with spatial scales X. Note down other parameters .... The grid partitioning is more intricate as the reservoir geometry is obviously more complex than the synthetic test cases, and it is likely that the layering is not perpendicular to the flow direction. In addition, history-matching of the migrating CO2 plume indicates that the formation contains significant in-layer heterogeneities [44]. Hence, harmonic average is not the correct upscaling of permeability. However, since finding a correct upscaling method is not trivial [28], we assume that the layering is close to perpendicular to the flow direction and retain the harmonic average.

The physical parameters are chosen based on the study [13] of CO2 migration through shale barriers in the Utsira formation. Particularly, the entry pressure is set low to better reproduce observed plume shapes from seismic images, in accordance with [13].

7 Results

Maybe merge this section with numerical simulations ??

7.1 Single horizontal semi-permeable layer

The simplest test case comprising a single semi-permeable layer with an open "chimney" is performed for two different petrophysical settings. In the first one we set a transmissibility multiplier of 10^{-8} for the semi-permeable layer to approximate it as fully sealing. The solutions after injection and towards the end of migration are shown in Figure 18.

During injection, there is a balance between CO2 accumulating below the sealing layer and CO2 exiting through the open "chimney". The thickness and shape of the plume under the sealing layer corresponds well between the full-dimensional model and the hybrid model. We
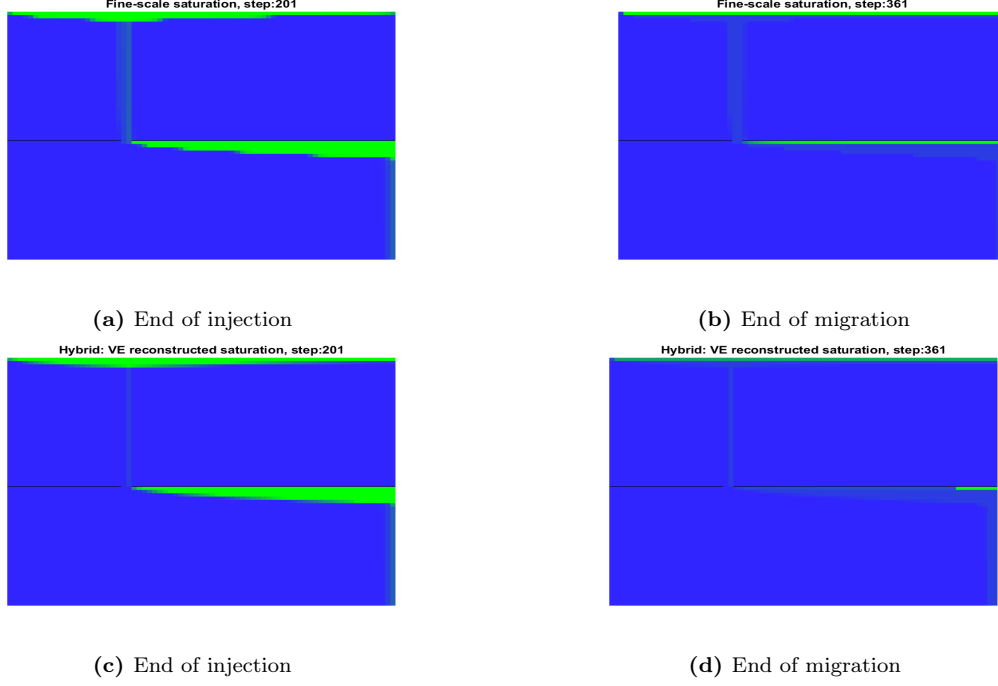
56

(a) End of injection **(b)** End of migration

(c) End of injection **(d)** End of migration

Figure 18: Comparison of CO2 saturation for a full-dimensional and hybrid model for a 2D domain with a single horizontal semi-permeable layer embedded in a high-permeable region.

note that residual saturation left behind in the vertical passage through the chimney, modeled as a veHorizontal transition region, is captured by the hybrid model. However, the horizontal extent of the residual part is larger in the full-dimensional model than the hybrid model, This is a direct consequence of the VE assumption applicable for cells in veHoriontal transition regions. CO2 exiting through the open chimney is assumed to be instantaneously segregated with the resident brine and thus immediately moves to the top of the formation. In other words, the horizontal component of the flux through the chimney is ignored by the hybrid model so that the residual part is only one column wide.

On the other hand, during late migration, there are notable differences between the models in saturation immediately below the sealing layers. In the fine-scale model, CO2 saturation is approximately at the maximum value $s_n = 1 - s_{wr}$ here, while it is significantly lower in the hybrid model. Once injection ceases, the pressure drop induces horizontal spreading and the plume equilibrates as a layer thin enough to only be represented by a single cell in the vertical direction. The fact that a full-dimensional model is limited by the vertical resolution, the accuracy of the solution is sensitive to sudden changes in saturation [41], as is characteristic for sharp-interface models. For VE columns in the hybrid model though, the sharp interface between CO2 and brine is given by an analytical expression, yielding a "correct" averaged reconstructed saturation in the fine cells [41]. The sensitivity to vertical resolution of the full-dimensional model is substantiated

in the post-injection stage since topography of low-permeable layers is the only effect opposing gravity [30]. As these layers are horizontal in our setup, the calculation of the vertical location of the sharp interface is vulnerable to errors.
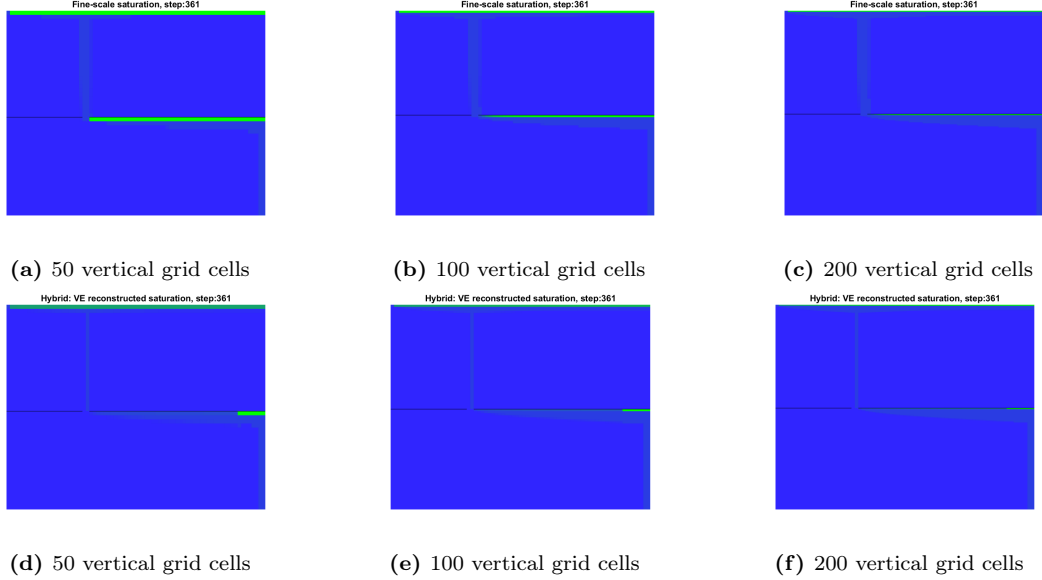

(a) 50 vertical grid cells   **(b)** 100 vertical grid cells   **(c)** 200 vertical grid cells

(d) 50 vertical grid cells   **(e)** 100 vertical grid cells   **(f)** 200 vertical grid cells

Figure 19: CO_2 saturation after migration for three different vertical resolutions, illustrating how the vertical saturation in VE columns of a full-dimensional model converges to the solution for the hybrid model as the vertical resolution is refined. First row: full-dimensional model. Second row: hybrid model.

To demonstrate the effect vertical resolution has on the location of the sharp interface, we conduct three simulations of increasing vertical resolution. The relative permeability function is linear to accentuate the differences caused by grid resolution. Saturation distributions at the end of simulation is shown in Figure 19, and exited volumes of CO_2 as a function of time is shown in Figure 20. During injection, the difference between the models is minor. After injection ceases, particularly beyond time step 250, the models diverge and eventually flatten. The discrepancy is due to the limited vertical resolution of the fine model not properly capturing the diffusive horizontal spreading from the parabolic term in 18. For the vertical resolutions shown in Figure 19, the sharp interface is less than one cell thick and its true height is not accurately resolved. By increasing the vertical resolution, the convex shape of the accumulated layer of CO_2 is better reproduced and the full-dimensional model converges to that predicted by the analytical expression from the hybrid model. Moreover, the fully saturated cell layer below the semi-permeable layer vanishes as the vertical resolution is refined, consistent with the analytically derived distribution in the hybrid model.

The second setting applies a transmissibility multiplier of 10^{-5} to facilitate diffuse leakage through the semi-permeable layer. The result is shown in Figure 21. Clearly, the reconstruc-

(a) 50 vertical grid cells

(b) 100 vertical grid cells

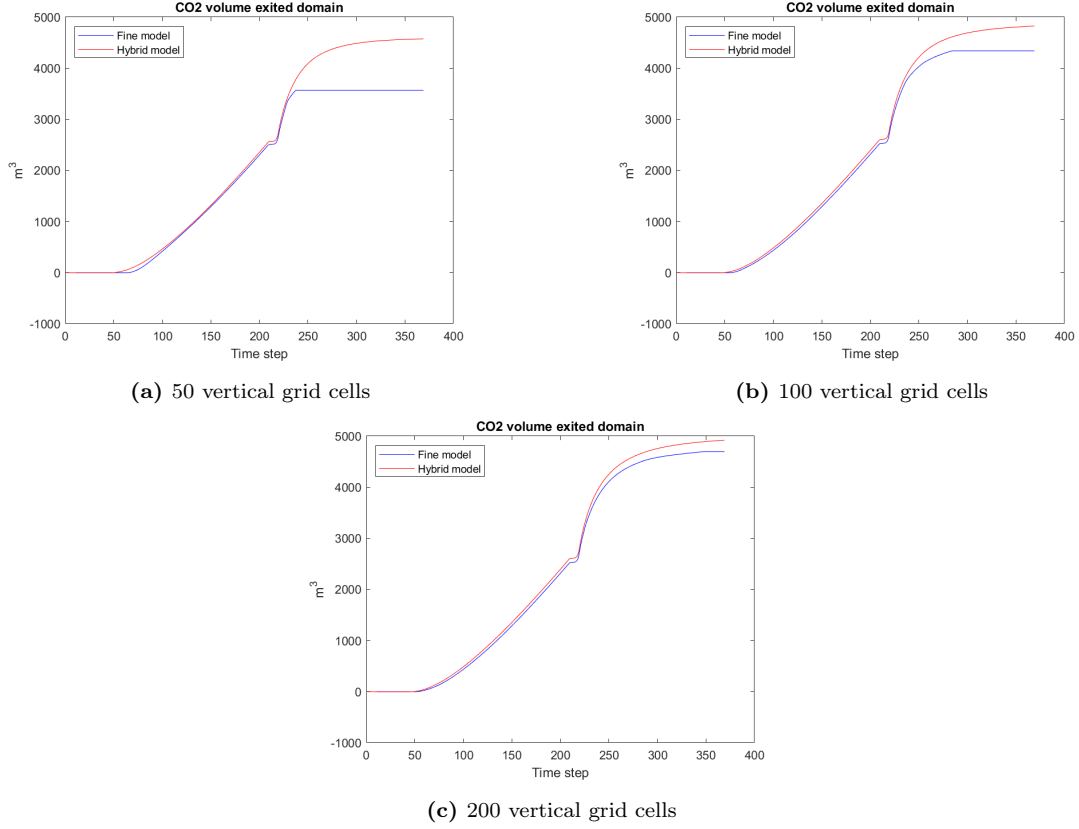**(c)** 200 vertical grid cells

Figure 20: Comparison of exited volume for three different vertical resolutions for the 2D horizontal test case with a single horizontal sealing layer.

tion procedure of the hybrid model is able to capture the slow vertical drainage through the semi-permeable layer, immobilized before reaching the caprock. The immobilized plume is more widespread in the full-dimensional model due to a greater amount of CO2 residing below the layer, responsible for a larger upward flux of CO2. Hence, differences in diffuse leakage is attributable to inaccuracies of the full-dimensional model close to the sharp interface.

A similar set of simulations are performed where the semi-permeable layer is represented as full-dimensional cells instead of faces, as detailed in section 5.1, and is shown in Figure 22. Diffuse leakage is now attributed to a capillary entry pressure rather than a transmissibility multiplier. The discrepancies between the fine and hybrid models are reminiscent of the simulations using a face representation. The full-dimensional model still suffers from insufficient vertical resolution to accurately resolve accumulated CO2 and subsequent migration through the semi-permeable layer. The spatial distribution of immobilized CO2 above the layer now reflects the entry pressure required for penetration, permeability and internal flow. The permeability for the semi-permeable layer is homogeneous though, hence the solution is less sensitive to flow
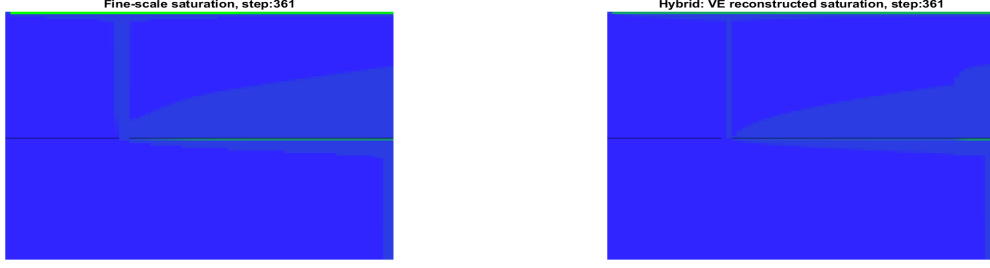
Figure 21: Comparison of full-dimensional and hybrid model for the 2D horizontal test case with a single horizontal semi-permeable layer represented as a face with transmissibility multiplier 10^{-5}. 100 cells are used in the vertical.
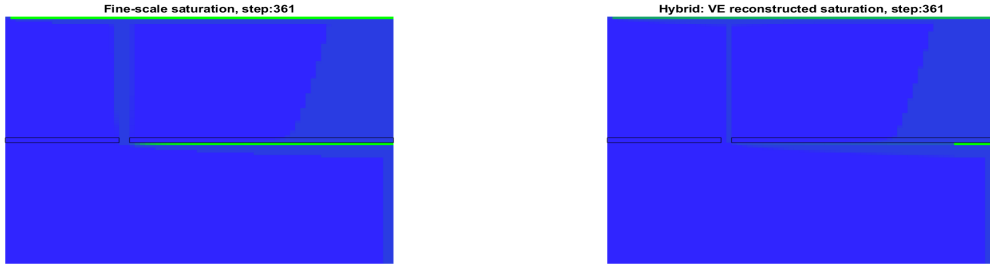

Figure 22: Comparison of full-dimensional and hybrid model for the 2D horizontal test case with a single horizontal semi-permeable layer represented as full-dimensional cells. 100 cells are used in the vertical.

internally in the layer, suggesting that representing the layer by a scaled transmissibility is sufficient in this simplified case.

7.2 Two-dimensional sloped domain

Not done. After talking with Odd, we made the conclusion that the purpose of this test case is to compare the new hybrid model with full-dim model where all possible transition zones are included, to verify that implementation of residual saturation is reliable.

7.3 Three-dimensional sloped domain

NB: THIS SUBSECTION WILL LIKELY BE SUBSTITUTED BY ANOTHER SETUP. Current results shown in Figure 23, 24 and 25, will thus be different but much of the discussion here will be retained.

At the end of injection (first column in Figure 23) we observe two distinct CO_2 plumes, a dominant one settling below the caprock and a smaller one residing below the lower semi-permeable layer. Both plumes are present in the hybrid model with a good correspondence in plume shape. The hybrid model also manages to trace the history of the plume, evident in the residual part below the upper semi-permeable layer. A noticeable difference is the gradual transition from zero to maximum CO_2 saturation for the top plume in the hybrid model. This becomes even clearer at the end of migration (second column in Figure 23) where we observe several cells that are fully saturated with CO_2 in the full-dimensional model, but have residual saturation in the hybrid model. This is mainly attributable to the limitations of too coarse vertical resolution.

The solution at the boundary of the domain contains limited information. The effect of retardation from semi-permeable layers becomes clear by extracting the solution from a cross-section of the grid, as shown in Figure 24 for the end of injection and end of simulation, respectively. For the former, the hybrid model correctly resolves accumulation of CO_2 below semi-permeable layers as well as diffuse leakage through the bottom semi-permeable layer, whose plume shape is in excellent agreement with the full-dimensional model. This test case illustrates the flaws of the hybrid model when modeling buoyant migration at the endpoints of semi-permeable layers, particularly around the coordinates (230, 150). The horizontal component of the flux at the endpoint is responsible for a diffuse spread of CO_2 in addition to buoyant migration. For the hybrid model though, the VE assumption is applicable in this area and imposes immediate vertical segregation, disregarding the horizontal spread. This discrepancy is substantiated at the end of the simulation where a larger part of the domain is covered by residual CO_2 for the full-dimensional model compared to the hybrid model. Another feature is that the hybrid model predicts a significantly taller plume at the left endpoint of the upper right semi-permeable layer, extending up to the caprock. This illustrates the fact that the VE assumption assigns all CO_2 to the neighboring VE column, immediately ascending, rather than distributing CO_2 in both principal directions. Hence, the hybrid model overestimates the vertical extent of these plumes by missing the diffuse component.

By combining the trap analysis from caprock, the semi-permeable layers and the remainders of the domain, we generate a trapping inventory for the simulated 400 years as shown in Figure 25. The graph shows that this is far from an optimal injection scenario, as the vast majority of injected CO_2 eventually exits the domain. As injection ceases after 40 years, remaining mobile CO_2 is forces into traps or out of domain, represented by an abrupt decrease in the free plume at this point. The residual part increases accordingly as migrating CO_2 leaves off an immobilized residual part.
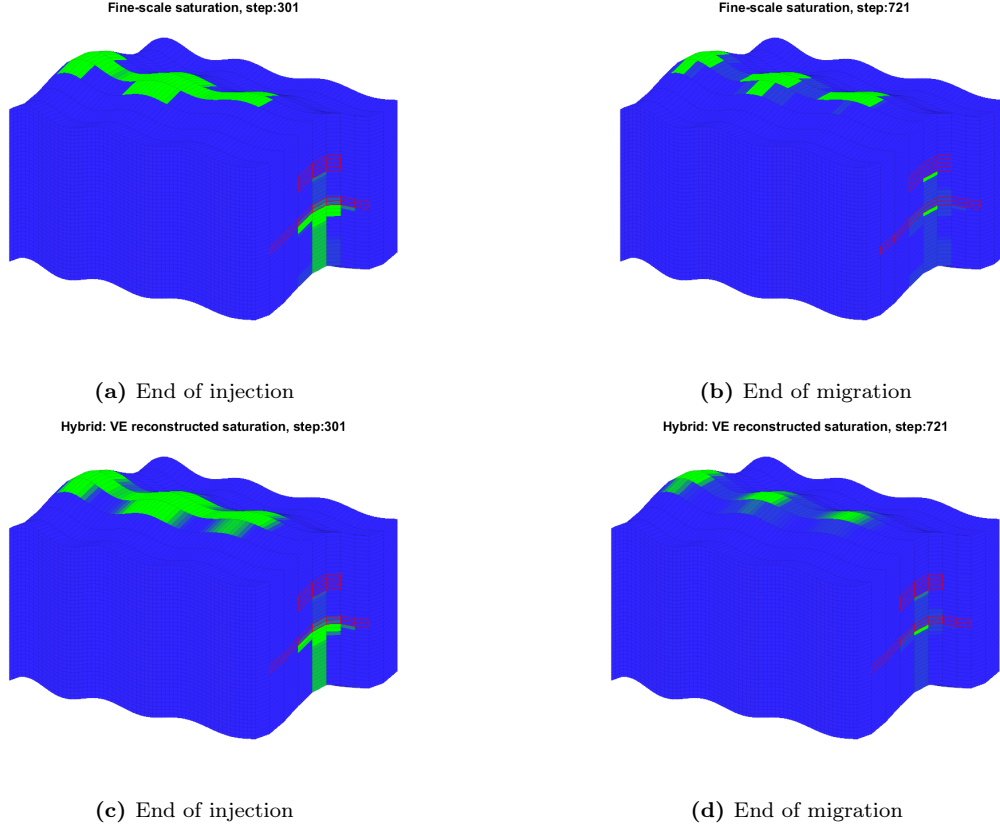
Figure 23: Comparison of CO2 saturation at end of injection and end of migration for the boundary of a synthetic sloped 3D domain. Semi-permeable layers (at boundary) marked in red.

8 Discussion

9 Conclusion

NOT FINISHED/READY !

Numerical simulation of long-term geological CO2 storage is severely limited by the combination of large spatial and temporal scales. Full-dimensional models are infeasible to run for a comprehensive study on three-dimensional real datasets, especially for stochastic simulations, and conventional VE models are primarily limited to simple homogeneous formations without in-layer heterogeneities [11]. Thus, hybrid models serve as a great tradeoff between the two methods in terms of accuracy and simulation time. Simulations on stochastic realizations of a 2D fictitious reservoirs reveals that the increase in accuracy of final saturation distribution prevails the decrease in simulation time compared to a VE model.

Hybrid models have been successfully implemented in MRST using a fully-implicit method with TPFA-MUP discretization in space [36]. The focus of this thesis has been to extend the
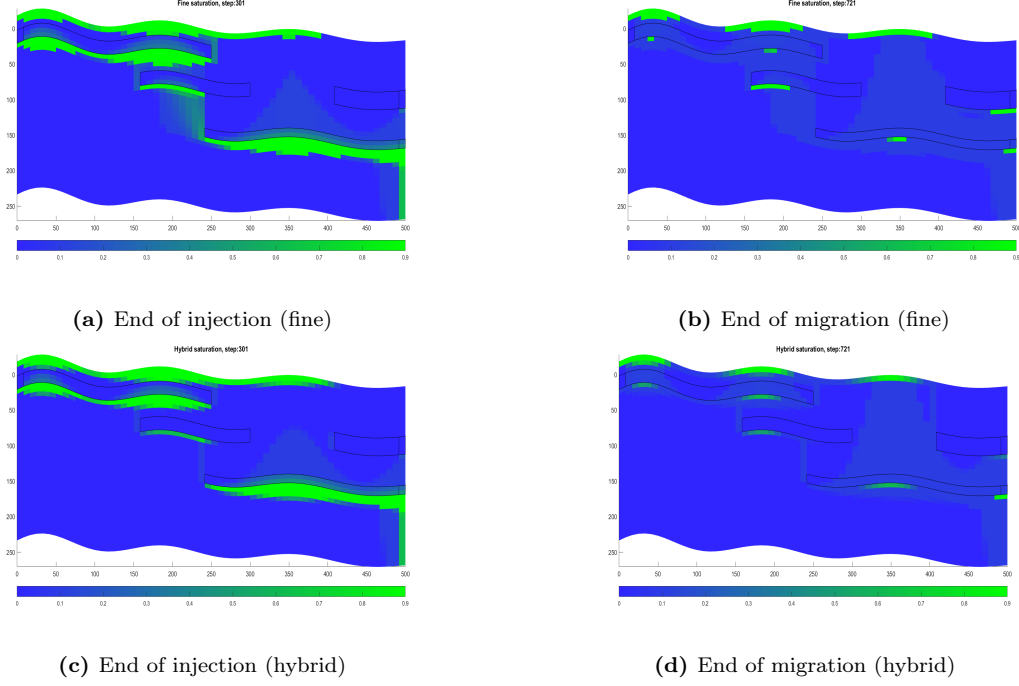
(a) End of injection (fine)

(b) End of migration (fine)

(c) End of injection (hybrid)

(d) End of migration (hybrid)

Figure 24: CO2 saturation at end of injection and end of migration for a 2D cross section in the xz-plane at $y = \max(y)/2$.

current hybrid framework with additional physical effects such as residual saturation and capillary pressure to facilitate more realistic simulation scenarios.

As VE models assume instantaneous segregation of CO2 and brine, the conventional framework with residual saturation is not able to resolve a scenario where the CO2 plume is immobilized before reaching the top of a column, and may yield large discrepancies with the full-dimensional solution. To cope with this, VE columns with non-zero bottom flux but with coarse scale saturation less than residual value - herein labeled NVE columns - have been modified. Despite not being in vertical equilibrium, NVE columns are still modeled with reduced dimensionality as they are destined to eventually become VE columns unless the plume is immobilized. Hence, introduction of NVE cells adds minor computational cost to the simulation. With these modifications, immobilized plumes are captured by the extended hybrid model as residually saturated CO2 and generally agrees well with the full-dimensional model.

The extended hybrid model has also been applied on a real 3D section of the Utsira formation, a scenario where a full-dimensional model is impractical due to extreme runtimes. Continue summary of results on 3D dataset ...

The hybrid model is still subject to improvement, particularly in terms of flexibility. In the current framework, discretization regions have to be assigned a-priori with no possibility to adapt during simulation time, as studied by [9] and shown to be particularly useful for layered
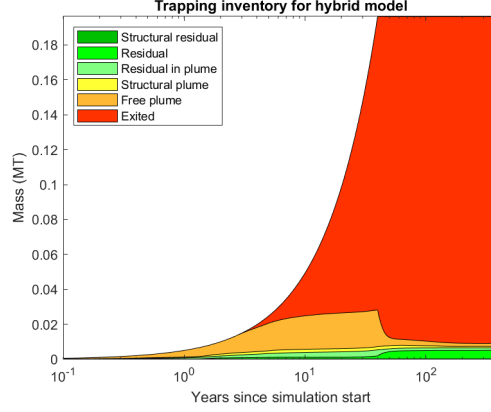
Figure 25: Trapping inventory for a synthetic sloped 3D domain simulating with a hybrid model.

heterogeneous formations, as studied in this thesis. If the layer permeabilities in the formation span a large interval, some layers are close to being in VE but is not adequately justified. In this case a resolution is to incorporate a multi-layer dynamic reconstruction (MLDR) to solve the vertical dynamics as an individual one-dimensional problem, as successfully implemented in [21] with the IMPES method. This strategy is unfortunately not possible in the fully-implicit method since the governing equations is solved as one monolithic system ??

On the other side, local heterogeneities *within* a layer are expected to have significant impact on the migration path of CO2 [13], but have not been accounted for in the high-permeable sandstones nor the low-permeable shales.

9.1 Model comparison

NOT SURE IF INCLUDING THIS

To quantify the discrepancies between the hybrid model and full-dimensional model we rely on simple statistical tools. An informative measure is the CO2 saturation mismatch for different discretization regions based on the absolute difference in saturation for the associated fine cells. The mean mismatch and variance is then given by,

$$\mu_{err,k} = \frac{1}{N_k} \sum_{i \in C_k} |s_{n,i} - \hat{s}_{n,i}|$$

$$\sigma^2_{err,k} = \frac{1}{N_k} \sum_{i \in C_k} \left(|s_{n,i} - \hat{s}_{n,i}| - \mu_{err,k} \right)^2$$

where C_k and N_k is the set and number of fine cells in discretization region k, respectively.

10 Improvements

Something to maybe mention in conclusion ...

While our hybrid model has shown great results multiple reservoir realizations compared to conventional VE models, it still lacks flexibility. A notable disadvantage is the static framework, including both preprocessing and simulation steps. Cells to be modeled as full-dimensional have to be specified manually by the user, and the assignment of cells and faces as sealing layers is too simplistic. Moreover, there are currently no options to dynamically change the discretization of cells during simulation time to update applicable VE regions. This has been implemented by [9] showing a large versatility and great agreement with the full-dimensional solution.

References

[1] Nurafiqah Abdullah et al. "The study of the effect of fault transmissibility on the reservoir production using reservoir simulation—Cornea Field, Western Australia". In: *Journal of Petroleum Exploration and Production Technology* 10.2 (Feb. 2020), pp. 739–753. ISSN: 2190-0566. DOI: 10.1007/s13202-019-00791-6. URL: https://doi.org/10.1007/s13202-019-00791-6.

[2] Takashi Akai et al. "Numerical modelling of long-term CO2 storage mechanisms in saline aquifers using the Sleipner benchmark dataset". In: *International Journal of Greenhouse Gas Control* 110 (2021), p. 103405. ISSN: 1750-5836. DOI: https://doi.org/10.1016/j.ijggc.2021.103405. URL: https://www.sciencedirect.com/science/article/pii/S1750583621001572.

[3] Ali Hasan Ali et al. "A Comparison of Finite Difference and Finite Volume Methods with Numerical Simulations: Burgers Equation Model". In: *Complexity* 2022 (June 2022), p. 9367638. ISSN: 1076-2787. DOI: 10.1155/2022/9367638. URL: https://doi.org/10.1155/2022/9367638.

[4] Odd Andersen. "Simplified models for numerical simulation of geological CO2 storage". PhD thesis. University of Bergen, 2017. URL: https://bora.uib.no/bora-xmlui/handle/1956/15477.

[5] Odd Andersen, Sarah Gasda, and Halvor Nilsen. "Vertically Averaged Equations with Variable Density for CO2 Flow in Porous Media". In: *Transport in Porous Media* (Dec. 2014), pp. 1–33. DOI: 10.1007/s11242-014-0427-z.

[6] Karl W. Bandilla, Michael A. Celia, and Evan Leister. "Impact of Model Complexity on CO2 plume modeling at Sleipner". In: *Energy Procedia* 63 (2014). 12th International Conference on Greenhouse Gas Control Technologies, GHGT-12, pp. 3405–3415. ISSN: 1876-6102. DOI: https://doi.org/10.1016/j.egypro.2014.11.369. URL: https://www.sciencedirect.com/science/article/pii/S1876610214021845.

[7] Karl W. Bandilla, Bo Guo, and Michael A. Celia. "A guideline for appropriate application of vertically-integrated modeling approaches for geologic carbon storage modeling". In: *International Journal of Greenhouse Gas Control* 91 (2019), p. 102808. ISSN: 1750-5836. DOI: https://doi.org/10.1016/j.ijggc.2019.102808. URL: https://www.sciencedirect.com/science/article/pii/S1750583619300684.

[8] J. Bear. *Dynamics of Fluids in Porous Media*. Dover Civil and Mechanical Engineering Series. Dover, 1988. ISBN: 9780486656755. URL: https://books.google.no/books?id=-XEaxd3hGzoC.

[9] Becker Beatrix et al. "An Adaptive Hybrid Vertical Equilibrium/Full-Dimensional Model for Compositional Multiphase Flow". In: *Water Resources Research* 58.1 (2022). e2021WR030990 2021WR030990, e2021WR030990. DOI: `https://doi.org/10.1029/2021WR030990`. eprint: `https://agupubs.onlinelibrary.wiley.com/doi/pdf/10.1029/2021WR030990`. URL: `https://agupubs.onlinelibrary.wiley.com/doi/abs/10.1029/2021WR030990`.

[10] Beatrix Becker et al. "A Pseudo Vertical Equilibrium Model for Slow Gravity Drainage Dynamics". In: *Water Resources Research* 53 (Nov. 2017). DOI: `10.1002/2017wr021644`.

[11] Beatrix Becker et al. "An Adaptive Multiphysics Model Coupling Vertical Equilibrium and Full Multidimensions for Multiphase Flow in Porous Media". In: *Water Resources Research* 54.7 (2018), pp. 4347–4360. DOI: `https://doi.org/10.1029/2017WR022303`. eprint: `https://agupubs.onlinelibrary.wiley.com/doi/pdf/10.1029/2017WR022303`. URL: `https://agupubs.onlinelibrary.wiley.com/doi/abs/10.1029/2017WR022303`.

[12] Yann Brenier and Jerome Jaffre. "Upstream Differencing for Multiphase Flow in Reservoir Simulation". In: *SIAM Journal on Numerical Analysis* 28.3 (1991), pp. 685–696. ISSN: 00361429. URL: `http://www.jstor.org/stable/2157723` (visited on 12/23/2022).

[13] Andrew J. Cavanagh and R. Stuart Haszeldine. "The Sleipner storage site: Capillary flow modeling of a layered CO2 plume requires fractured shale barriers within the Utsira Formation". In: *International Journal of Greenhouse Gas Control* 21 (2014), pp. 101–112. ISSN: 1750-5836. DOI: `https://doi.org/10.1016/j.ijggc.2013.11.017`. URL: `https://www.sciencedirect.com/science/article/pii/S1750583613004192`.

[14] M. A. Celia et al. "Status of CO2 storage in deep saline aquifers with emphasis on modeling approaches and practical simulations". In: *Water Resources Research* 51 (2015), pp. 6846–6892. DOI: `doi:10.1002/2015WR017609`.

[15] Benjamin Court et al. "Applicability of vertical-equilibrium and sharp-interface assumptions in CO2 sequestration modeling". In: *International Journal of Greenhouse Gas Control* 10 (2012), pp. 134–147. ISSN: 1750-5836. DOI: `https://doi.org/10.1016/j.ijggc.2012.04.015`. URL: `https://www.sciencedirect.com/science/article/pii/S1750583612001041`.

[16] *Effects of Data Resolution: Estimation of Trap Analysis Accuracy.* `https://www.sintef.no/projectweb/mrst/modules/co2lab/traps/estimation-of-trap-analysis-accuracy/`. 2013. Accessed: 21.12.2022.

[17] S. E. Gasda, J. M. Nordbotten, and M. A. Celia. "Vertical equilibrium with sub-scale analytical methods for geological CO2 sequestration". In: *Computational Geosciences* 13.4 (Apr. 2009), p. 469. ISSN: 1573-1499. DOI: `10.1007/s10596-009-9138-x`. URL: `https://doi.org/10.1007/s10596-009-9138-x`.

[18] Sarah E. Gasda, Jan M. Nordbotten, and Michael A. Celia. "The impact of local-scale processes on large-scale CO2 migration and immobilization". In: *Energy Procedia* 4 (2011). 10th International Conference on Greenhouse Gas Control Technologies, pp. 3896–3903. ISSN: 1876-6102. DOI: https://doi.org/10.1016/j.egypro.2011.02.327. URL: https://www.sciencedirect.com/science/article/pii/S1876610211006060.

[19] Sarah E. Gasda, Jan M. Nordbotten, and Michael A. Celia. "The impact of local-scale processes on large-scale CO2 migration and immobilization". In: *Energy Procedia* 4 (2011). 10th International Conference on Greenhouse Gas Control Technologies, pp. 3896–3903. ISSN: 1876-6102. DOI: https://doi.org/10.1016/j.egypro.2011.02.327. URL: https://www.sciencedirect.com/science/article/pii/S1876610211006060.

[20] B. Guo et al. "A vertically integrated model with vertical dynamics for CO2 storage". In: *Water Resources Research* 50 (2014), pp. 6269–6284. DOI: doi:10.1002/2013WR015215.

[21] Bo Guo. PhD thesis. Princeton University, 2016. URL: http://arks.princeton.edu/ark:/88435/dsp01w0892d35w.

[22] Bo Guo et al. "Flow regime analysis for geologic CO2 sequestration and other subsurface fluid injections". In: *International Journal of Greenhouse Gas Control* 53 (2016), pp. 284–291. ISSN: 1750-5836. DOI: https://doi.org/10.1016/j.ijggc.2016.08.007. URL: https://www.sciencedirect.com/science/article/pii/S1750583616304698.

[23] Nilsen H.M., Lie KA., and Andersen O. "Fully-implicit simulation of vertical-equilibrium models with hysteresis and capillary fringe". In: *Computational Geosciences* 20 (2016), pp. 49–67. DOI: https://doi.org/10.1007/s10596-015-9547-y. URL: https://link.springer.com/article/10.1007/s10596-015-9547-y.

[24] Nilsen H.M., Lie KA., and Andersen O. "Robust simulation of sharp-interface models for fast estimation of CO2 trapping capacity in large-scale aquifer systems." In: *Computational Geosciences* 20 (2016), pp. 93–113. DOI: 10.1007/s10596-015-9549-9. URL: https://link.springer.com/article/10.1007/s10596-015-9549-9.

[25] Herbert E. Huppert and Jerome A. Neufeld. "The Fluid Mechanics of Carbon Dioxide Sequestration". In: *Annual Review of Fluid Mechanics* 46.1 (2014), pp. 255–272. DOI: 10.1146/annurev-fluid-011212-140627. eprint: https://doi.org/10.1146/annurev-fluid-011212-140627. URL: https://doi.org/10.1146/annurev-fluid-011212-140627.

[26] Ruben Juanes, Christopher W. MacMinn, and Michael L. Szulczewski. "The Footprint of the CO2 Plume during Carbon Dioxide Storage in Saline Aquifers: Storage Efficiency for Capillary Trapping at the Basin Scale". In: *Transport in Porous Media* 82.1 (Mar. 2010), pp. 19–30. ISSN: 1573-1634. DOI: 10.1007/s11242-009-9420-3. URL: https://doi.org/10.1007/s11242-009-9420-3.

[27]   Hans Petter Langtangen. *Finite Difference Computing with Exponential Decay Models*. Lecture Notes in Computational Science and Engineering. Springer Cham, 2016. ISBN: 978-3-319-29439-1. DOI: `https://doi.org/10.1007/978-3-319-29439-1`.

[28]   Knut-Andreas Lie. *An Introduction to Reservoir Simulation Using MATLAB/GNU Octave: User Guide for the MATLAB Reservoir Simulation Toolbox (MRST)*. Cambridge University Press, 2019. DOI: `10.1017/9781108591416`.

[29]   Knut-Andreas Lie and Olav Møyner. *Advanced Modeling with the MATLAB Reservoir Simulation Toolbox*. Cambridge University Press, 2021. DOI: `10.1017/9781009019781`.

[30]   I. S. Ligaarden and Halvor Møll Nilsen. "Numerical Aspects of Using Vertical Equilibrium Models for Simulating CO2 Sequestration". In: 2010.

[31]   Svein Linge and Hans Petter Langtangen. "Nonlinear Problems". In: *Finite Difference Computing with PDEs: A Modern Software Approach*. Cham: Springer International Publishing, 2017, pp. 353–407. ISBN: 978-3-319-55456-3. DOI: `10.1007/978-3-319-55456-3_5`. URL: `https://doi.org/10.1007/978-3-319-55456-3_5`.

[32]   Bert Metz et al. "Report: Carbon Dioxide Capture and Storage". In: (2005), p. 431.

[33]   Halvor Møll Nilsen et al. "Field-case simulation of CO2 -plume migration using vertical-equilibrium models". In: *Energy Procedia* 4 (2011). 10th International Conference on Greenhouse Gas Control Technologies, pp. 3801–3808. ISSN: 1876-6102. DOI: `https://doi.org/10.1016/j.egypro.2011.02.315`. URL: `https://www.sciencedirect.com/science/article/pii/S1876610211005947`.

[34]   Halvor Møll Nilsen et al. "Field-case simulation of CO2 -plume migration using vertical-equilibrium models". In: *Energy Procedia* 4 (2011). 10th International Conference on Greenhouse Gas Control Technologies, pp. 3801–3808. ISSN: 1876-6102. DOI: `https://doi.org/10.1016/j.egypro.2011.02.315`. URL: `https://www.sciencedirect.com/science/article/pii/S1876610211005947`.

[35]   Halvor Møll Nilsen et al. "Spill-point analysis and structural trapping capacity in saline aquifers using MRST-co2lab". In: *Computers Geosciences* 75 (2015), pp. 33–43. ISSN: 0098-3004. DOI: `https://doi.org/10.1016/j.cageo.2014.11.002`. URL: `https://www.sciencedirect.com/science/article/pii/S0098300414002520`.

[36]   Olav Møyner and Halvor Møll Nilsen. "Multiresolution coupled vertical equilibrium model for fast flexible simulation of CO2 storage". In: *Computational Geosciences* 23 (2019), pp. 1–20. DOI: `https://doi.org/10.1007/s10596-018-9775-z`. URL: `https://link.springer.com/article/10.1007/s10596-018-9775-z`.

[37]   *MRST: Transforming research on reservoir simulation*. `https://www.sintef.no/projectweb/mrst/`. Accessed: 21.12.2022.

[38] J. M. Nordbotten and H. K. Dahle. "Impact of the capillary fringe in vertically integrated models for CO2 storage". In: *Water Resources Research* 47.2 (2011). DOI: https://doi.org/10.1029/2009WR008958. eprint: https://agupubs.onlinelibrary.wiley.com/doi/pdf/10.1029/2009WR008958. URL: https://agupubs.onlinelibrary.wiley.com/doi/abs/10.1029/2009WR008958.

[39] Jan M. Nordbotten and Michael A. Celia. *Geological Storage of CO2: Modeling Approaches for Large-Scale Simulation.* John Wiley & Sons, 2012. ISBN: 9780470889466.

[40] *Top-Surface Grid Tutorial.* https://www.sintef.no/projectweb/mrst/modules/co2lab/traps/show-top-surface1/. 2011. Accessed: 21.12.2022.

[41] *Vertical-Equilibrium Models.* https://www.sintef.no/projectweb/mrst/modules/co2lab/ve-models/. 2014. Accessed: 21.12.2022.

[42] Francesca Watson, Odd Andersen, and Halvor Nilsen. "Rapid Optimization of the New Sleipner Benchmark Model". In: Sept. 2021.

[43] Mark Wilkinson et al. "CO2Mineral Reaction in a Natural Analogue for CO2 Storage–Implications for Modeling". In: *Journal of Sedimentary Research - J SEDIMENT RES* 79 (July 2009). DOI: 10.2110/jsr.2009.052.

[44] G.A. Williams and R.A. Chadwick. "Influence of reservoir-scale heterogeneities on the growth, evolution and migration of a CO2 plume at the Sleipner Field, Norwegian North Sea". In: *International Journal of Greenhouse Gas Control* 106 (2021), p. 103260. ISSN: 1750-5836. DOI: https://doi.org/10.1016/j.ijggc.2021.103260. URL: https://www.sciencedirect.com/science/article/pii/S1750583621000128.

[45] Zhibing Yang et al. "Modeling Immiscible Two-Phase Flow in Rough Fractures From Capillary to Viscous Fingering". In: *Water Resources Research* 55.3 (2019), pp. 2033–2056. DOI: https://doi.org/10.1029/2018WR024045. eprint: https://agupubs.onlinelibrary.wiley.com/doi/pdf/10.1029/2018WR024045. URL: https://agupubs.onlinelibrary.wiley.com/doi/abs/10.1029/2018WR024045.

[46] Tianyuan Zheng, Bo Guo, and Haibing Shao. "A hybrid multiscale framework coupling multilayer dynamic reconstruction and full-dimensional models for CO2 storage in deep saline aquifers". In: *Journal of Hydrology* 600 (2021), p. 126649. ISSN: 0022-1694. DOI: https://doi.org/10.1016/j.jhydrol.2021.126649. URL: https://www.sciencedirect.com/science/article/pii/S0022169421006971.